



Science Arts & Métiers (SAM)

is an open access repository that collects the work of Arts et Métiers Institute of Technology researchers and makes it freely available over the web where possible.

This is an author-deposited version published in: <https://sam.ensam.eu>
Handle ID: [.http://hdl.handle.net/10985/24001](http://hdl.handle.net/10985/24001)

To cite this version :

D. DEPRIESTER, Jean-Patrick GOULMY, Laurent BARRALLIER - Crystal Plasticity simulations of in situ tensile tests: A two-step inverse method for identification of CP parameters, and assessment of CPFEM capabilities - International Journal of Plasticity - Vol. 168, p.103695 - 2023

Any correspondence concerning this service should be sent to the repository

Administrator : scienceouverte@ensam.eu



Crystal Plasticity simulations of in situ tensile tests: a two-step inverse method for identification of CP parameters, and assessment of CPFEM capabilities

D. Depriester^{a,*}, J.P. Goulmy^a and L. Barrallier^a

^aArts et Métiers Institute of Technology, MSMP, HESAM Université, F-13617 Aix-en-Provence, France

ARTICLE INFO

Keywords:

DIC
in situ tensile test
EBSD
Crystal Plasticity
CPFEM

Abstract


As the computational capability of modern computers increases, the Crystal Plasticity Finite Element Method (CPFEM) becomes more and more popular in materials science to model the mechanical behaviour of polycrystals. Indeed, such analysis provides extensive information about local mechanical fields (such as plastic strain and stress), which can be useful for understanding the behaviour of bulk materials. However, estimating the parameters of the CP constitutive laws is still challenging because they are not directly related to the macroscopic behaviour of the polycrystalline aggregates. Thus, one way to identify such parameters is by inverse analysis from CPFEM simulations. However, such approach is usually extremely time consuming. This paper proposes a two-step optimization scheme to determine these coefficients. The first step is based on a simple model, similar to that proposed by Sachs back in 1928. The second step is based on CPFEM simulations, to be compared with experimental data acquired by an in situ tensile test and full-field measurements made by High-Resolution Digital Image Correlation (HRDIC). The uniqueness of the solution found by inverse analysis is studied and ways to solve the local minima issues are provided. Finally, the ability of CPFEM to replicate an in situ tensile test is assessed.

1. Introduction

Recent advances in computational power together with an increasing interest in micro-engineering has led to the emergence of micromechanical analysis. It consists in analysing the behaviour of materials at their microscopical scale, when undergoing mechanical loads. When dealing with polycrystals, this study area often deals with the plastic deformation at grain scale, and is usually referred to as Crystal Plasticity (CP) analysis. For instance, understanding the plastic behaviour at grain scale of such materials is of great interest for prediction of creep (?) or fatigue behaviour (??). However, because of the small characteristic size of the strain heterogeneities (few micrometers) and the inherent anisotropy of the crystalline materials, estimation of the local plastic activity is still very challenging, although it can be addressed either experimentally or by numerical simulation.

Digital Image Correlation (DIC) is a means to get full-field measurements of a strained sample. At microscopic scale, DIC is usually performed during in situ tensile test in the chamber of Scanning Electron Microscope (SEM). Although stereographic DIC is now commonly used in the literature to get the full 3D displacement fields, this technique is only restricted for optical photographs. Hence, SEM-DIC is almost always performed in 2D, and plane

*Corresponding author

 dorian.depriester@ensam.eu (D. Depriester); jean-patrick.goulmy@ensam.eu (J.P. Goulmy); laurent.barrallier@ensam.eu (L. Barrallier)

ORCID(s): 0000-0002-2881-8942 (D. Depriester); 0000-0002-7963-3825 (J.P. Goulmy); 0000-0001-7684-6625 (L. Barrallier)

strain assumption is usually made in this case (??). In (?), the present authors performed an in situ tensile test on commercially pure copper. Electron Backscattered Diffraction (EBSD) was used to characterize the grains in terms of shapes and crystalline orientations. Thanks to the rough surface of the sample (due to slight chemical etching), High-Resolution DIC (HRDIC) was performed from SEM images (?), evidencing localization bands within each grain. These bands were 100 to 200 nm thick and no correlation between their orientations and the loading direction was evidenced. However, it was shown that these orientations were related to the crystalline orientation of the grains. Indeed tracking the active slip system (SS) in each grain, assuming an homogeneous tensile stress, resulted in very good prediction of slip activity, when compared to experimental data. It is worth mentioning that ? have recently published a new method to automatically identify the slip activity from SEM-DIC measurements. This method relies on the identification of active SSs by locally matching the measured displacement with the theoretical kinematic of all SSs, given by the local crystallographic orientation.

Crystal Plasticity Finite Element Methods (CPFEM) is now widely used in the literature to simulate the plastic behaviour of crystalline materials. Nevertheless, one key issue when performing such simulation is the estimation of constitutive laws parameters. Indeed, the evaluation of mechanical behaviour at the grain scale is not straightforward because there is no standard mechanical test at this scale. ? were the first to introduce the so-called “trace method” to identify the Critical Resolved Shear Stress (CRSS); this method essentially relies on statistical analyses of slip traces appearing in cross sections, which can be related to the macroscopic stress and thus to their ease of activation. More recently, ? and ? took advantage of recent advances in High-Energy X-ray Diffraction Microscopy (HEDM) to estimate the CRSSs of the hexagonal phase of titanium alloys from 3D images of bulk materials undergoing tensile loading. One way to perform mechanical tests at crystal scale is based on the micrometer-scaled pillar compression tests (????) or from single-crystal nano-indentation tests coupled with CPFEM modelling and optimization techniques (???). However, ? showed that, in the case of hexagonal phases, the HEDM-based method was more accurate than techniques based on slip traces or nano-indentations. An alternative way to identify CP parameters is to use CPFEM to simulate bulk-scaled mechanical tests and use inverse analysis to characterize the local behaviour. For instance, ? used the macroscopic tensile curve to identify the CP parameters of bainite steel. However, different CP parameters can result in the same tensile curve (???); hence the need to perform the inverse analysis on local fields as well, as demonstrated by ? about nano-indentation. For in situ tensile test, ? proposed to minimize a mixture of a macroscopic cost function (based on tensile curve) and a microscopic one (based on the strain measurements, thanks to DIC). ? proposed a similar approach but used the displacement field to define the microscopic cost function whereas ? used the local stresses, experimentally measured by High Resolution EBSD (HREBSD). Alternatively, ? used three different macroscopic stress-strain curves, obtained from compression-tension, uniaxial tension and cyclic loading tests, to estimate the CP parameters of Mg-4Al alloy. Still, because of the inherent non-linearity of CPFEM and the

numerous Degrees Of Freedom (DOFs) it involves, CPFEM usually takes days to complete, hence the difficulty to run optimization loops within a reasonable time. In addition, the CP parameters depend on the chemical composition of the studied material, but also on its grain size distribution. Indeed, ? determined CP parameters of 316LN stainless steels in different metallurgical conditions; evidencing that these parameters were sensitive to the grain sizes, with good consistency with the well-known Hall-Petch relationship.

Another issue when one tries to perform CPFEM lies in the definition of boundary conditions (BCs) to be applied on the mesh. Indeed, ? showed that conventional BCs (e.g. fixed surface) leads to overconstrained grains at the vicinity of boundaries. In order to avoid such artefact, ? only considered grains away from the boundaries in their analysis. ? and ? used a surrounding medium whose mechanical behaviour was governed by the average stress–strain curve. If the simulation is intended to replicate an in situ tensile test, an alternative method is to prescribe the actual displacement field measured by DIC as BCs (DICBCs). ? reported that the localization pattern was more realistic when using DICBCs than when using homogeneous BCs.

CPFEM can be applied either on 3D Representative Volume Elements (RVEs), usually randomly generated using Voronoi-like tessellations (???????) or a dedicated software (??), or from 2D meshes generated from EBSD maps (??????). Using 3D RVEs allows to perform full 3D computations, but their generation usually relies on a statistical description of the aggregate (grain size distribution, crystallographic texture...). On the other hand, EBSD-based meshes are more realistic because they replicate the actual grain morphologies and crystallographic orientations, and they allow to compare the local fields (e.g. displacement) between the simulations and the experiment. Because the meshed geometry corresponds to the imaged surface, and because of the small thickness of in situ tensile samples, the mesh surfaces parallel to the imaged surface are usually considered as stress-free (????), and the interaction between the apparent and the sub-surfaced grains are usually neglected, leading to near plane-stress assumption. Indeed, ? showed that this was a fair approximation when one wants to study the strain on the free surface, but they also showed that the aforementioned interaction can impair the slip activity. Conversely, ? showed that the strain was slightly higher when an underneath layer of random orientations was added, compared to single-layered CPFEM simulations; although they reported similar strain distributions in both cases. Under the near plane-stress assumption, grains are usually modelled columnar with an arbitrary thickness. ? reported that the number of elements in thickness (along the out-of-plane direction) had little to no effect on the CPFEM results. ? reported that EBSD-based simulations lead to more realistic strain values than simulations performed on random 3D aggregates; conversely, the latter lead to more realistic crystalline reorientations. Concerning the element type to be used in CPFEM, ? showed that quadrangular elements (in 2D) were able to capture the macroscopic shear bands in polycrystals, whereas triangular element were not. Still, to the best authors' knowledge, the submicrometer-thick intragranular shear bands, as evidenced by SEM HRDIC (????), have never been simulated by CPFEM on polycrystals. Actually, these bands are usually not considered in

CPFEM analyses because of their very small thickness, compared to the typical element size. However, ? suggested that simulating such phenomenon would require special numerical techniques, such as that proposed by ?. ? used CPFEM to simulate the tensile test of α titanium. They showed that the strain was heterogeneous even at early stage of the deformation (near the yield point), but that this strain was even more heterogeneous at larger deformation.

A tool was recently developed to generate conforming meshes from EBSD data (?), namely MTEX2Gmsh. It takes advantage of the MTEX's grain reconstruction algorithm (?) and the Gmsh meshing software (?), resulting in smooth and well defined Grain Boundaries (GBs) together with limited DOFs.

Alternatively to CPFEM, the macroscopic behaviour of a polycrystalline aggregate in the elasto-plastic domain can be estimated using Fast Fourier Transforms (FFT) -based methods (e.g. ?, and references therein). These methods consider a regular grid as input data to solve the compatibility and the equilibrium equations locally in the Fourier space. Visco-Plastic Self-Consistent (VPSC) models (??) can also be used to estimate the macroscopic behaviour of a polycrystalline aggregate, given the local mechanical constitutive laws (e.g. crystal plasticity). These models use an iterative scheme to simulate the behaviour of the aggregates when surrounded by the homogenized medium. ? used a combination of nanoindentation tests coupled with CPFEM-based inverse analysis, and FFT-based methods to evaluate the CP parameters of dual phase DP1000 steel. Both FFT-based methods and VPSC models are very fast compared to CPFEM (e.g. ?), but CPFEM is more suited for investigation of phenomena occurring at grain and sub-grain scales (?); in addition, it can be extended to more complex cases, such as crack nucleation (??), fracture (???), void growth (?) or phase transformation (?). It is worth mentioning that ? recently proposed a promising Convolutional Neural Network (CNN) -based CPFEM to circumvent the expensive computational time.

As seen above, CPFEM is now commonly used by researchers to replicate an in situ tensile test, although the underlying assumption of the related analyses are quite different (e.g. plane strain for DIC vs. near plane stress for CPFEM). In addition, the estimation of CP parameters is not straightforward. Hence, the two following questions arise:

- How can we estimate the CP parameter from a tensile test?
- How confident can we be about the replication of a tensile with the aid of CPFEM?

Thus, the aim of this paper is twofold. The first objective is to propose a method to estimate the CP parameters within a reasonable time. The robustness of the proposed approach (named two-step method hereafter) must be evaluated. The second objective is to quantitatively evaluate the ability of CPFEM to replicate the plastic deformation occurring at grain scale and investigate the relevancy of equivalent strain descriptors commonly used in DIC.

As a result, this paper divides as follows. Section 2 introduces the material used in this work, whereas section 3 recalls the base equations used in CP simulations. In section 4, a simple CP model, similar to that of ?, is proposed.

This model allows to quickly have a first sight on the optimal parameters for CPFEM. In section 5, these parameters are optimized through an inverse analysis scheme, based on the comparison between the experimental and the numerical results given by CPFEM, in terms of macroscopic stress and displacement field. Finally, the models and methods are examined to assess their limitations and offer helpful recommendations to readers who are interested in CPFEM simulations and CPFEM-based inverse analyses.

2. Material

In (?), an in situ tensile test was performed on commercially pure copper. The Region of Interest (RoI) was imaged by SEM and EBSD. Figure 1 illustrates the 115 reconstructed grains in the RoI, whereas Figure 2 shows the macroscopic tensile curve (blue dots). The tensile test was performed along the horizontal axis of Figure 1, denoted

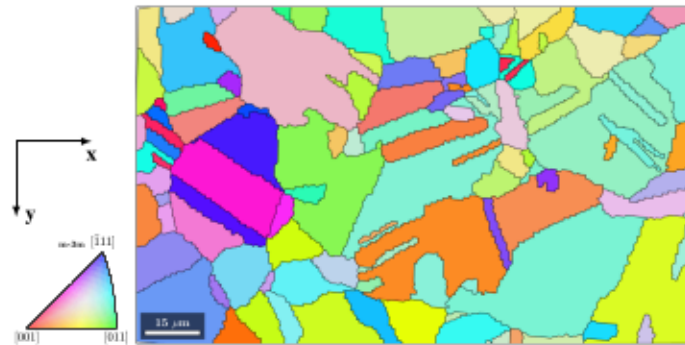


Figure 1: Reconstructed grains: the colour relates to the mean orientation of each grain.

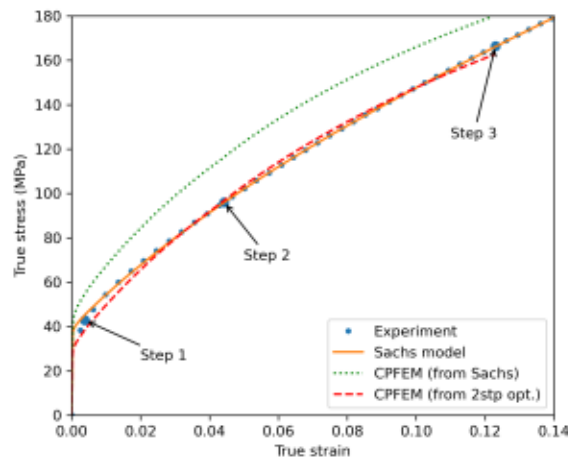


Figure 2: Tensile curves obtained either from in situ experiment (?), Sachs model (section 4) or CPFEM simulations (section 5). The green dotted curve is obtained when performing CPFEM simulation using CP parameters identified through the Sachs model, whereas the red dashed curve is obtained by CPFEM-based optimization. Steps refer to points where DIC measurements were made.

x below. HRDIC analyses were made from stitched SEM images at three deformation stages (called steps in ref.).

These steps are recalled in Figure 2 (see arrows). Figure 3 shows the results from DIC, in terms of apparent equivalent strain, depending on the window size used for DIC (denoted φ). In the context of DIC, the window size indicates

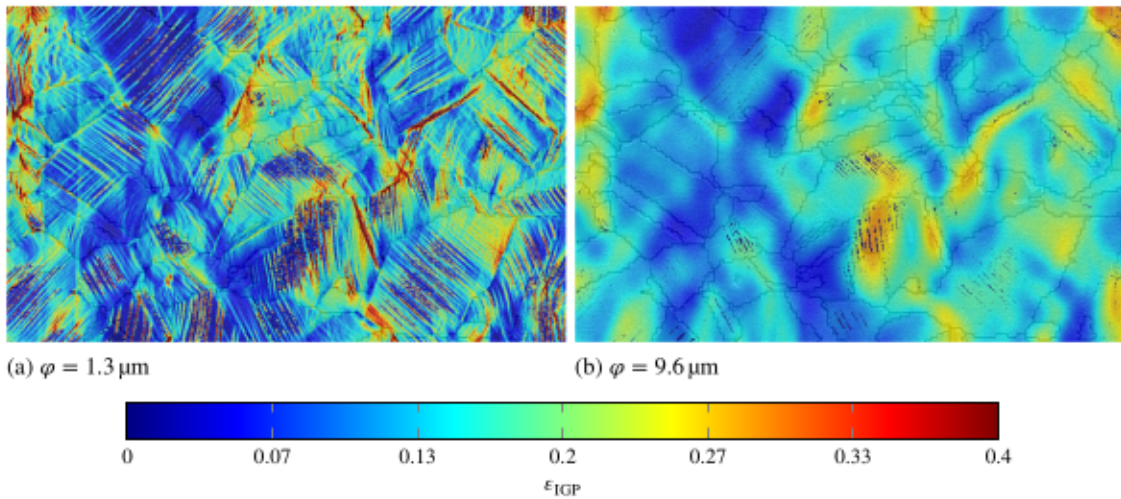


Figure 3: Results from DIC (step 3): values of ϵ_{IGP} (4) depending on the window size (φ) (?).

the size of the area of influence of a pixel value over the measured strain at surrounding locations (see details in (??)). The experimental approach allowed successively: to define the DIC parameters to be used to evidence the strain heterogeneities in the grains, to define the RoI and to analyze the results obtained in this area. As a conclusion, two DIC windows should be used depending on the observations one wishes to make. The DIC window must be of the order of 10 times the width of the slip bands if one wants to visualize them; the DIC window must be of the order of the grain size when the objective is to compare the results with modelling and visualize strain heterogeneities between grains. As a result, a window size $\varphi = 1.3 \mu\text{m}$ was chosen to detect intragranular localization bands (Fig. 3a), and a window size $\varphi = 9.6 \mu\text{m}$ was chosen to compare strain fields with the model (Fig. 3b). In Figure 3a, it appears, at a first sight, that some grains undergo simple slip; whereas others undergo double shear. However, it is worth mentioning that two SSs can share the same slip trace (??). Thus, simple traces can in fact denote double slip; and double traces can denote double, triple or quadruple slip. The SEM and EBSD analyses did not reveal any evolution of grain boundaries (such as dynamic recovery or grain boundary sliding).

In (?), the texture evolution was first computed from a large EBSD map (consisting in 450 grains) and then recomputed from reduced EBSD data in order to study the influence of the number of considered grains on the texture evolution estimation. It was shown that 50 grains were enough to evidence the texture evolution induced by a tensile test on pure copper. Therefore, data from all the 115 grains (illustrated in Figure 1) were considered in this work.

3. Theory

3.1. Localization criterion in SEM DIC

This subsection describes the criterion used in literature to evidence localization bands in SEM DIC.

Given the displacement field (denoted \mathbf{u} hereafter) measured by DIC, one can compute the gradient tensor, denoted \mathbf{F} below. Using the index notation, it is defined such that:

$$F_{ij} = \frac{\partial u_i}{\partial X_j} + \delta_{ij}. \quad (1)$$

In (1), X_j is the coordinate along the j -th axis of a given point in initial configuration, whereas δ_{ij} is the Kronecker delta. During in situ tensile tests, DIC measurements cannot be performed at each strain increment, mainly because each DIC measurement can take minutes to complete (for instance, in (?), each High-Resolution stitched SEM image required about one hour to get). Thus, the full loading path is rarely collected by SEM DIC and the equivalent strain (integrated over all the straining path) cannot be computed. In addition, since DIC can be performed on the imaged surface only, out-of-plane components of \mathbf{F} cannot be measured. Hence, the need for “partial” descriptors of plastic activity. For metallic materials, ? have introduced the “effective” shear strain:

$$\gamma_{\text{eff}} = \sqrt{(F_{11} - F_{22})^2 + (F_{12} + F_{21})^2} \quad (2)$$

This definition assumes plane strains to compute the maximum shear strain. Although the latter authors conceded that the hypotheses behind (2) were questionable, they showed that this criterion can be used to evidence the localization bands from in situ DIC. They also showed that these bands were parallel to the traces of SSs (intersection of slip plane with observation plane). Therefore, the orientation of the apparent localization bands provides valuable information about the active SSs within each grain of a polycrystal.

Under the simple shear assumption, ? have proposed the following relationship for estimating the equivalent strain based on the effective shear:

$$\epsilon_{\text{eff}} = \frac{\gamma_{\text{eff}}}{\sqrt{3}} \sqrt{1 + \frac{\gamma_{\text{eff}}^2}{3}} \quad (3)$$

However, the definition (2) for γ_{eff} works under the small strain assumption¹. Hence, the following equations were proposed by ? to estimate the von Mises equivalent strain, assuming a purely Isochoric Generalized Plane (IGP) strain:

$$\epsilon_{\text{IGP}} = \sqrt{\frac{2}{3}} \sqrt{\frac{(E_{11} - E_{22})^2 + (E_{11} - E_{33})^2 + (E_{22} - E_{33})^2}{3} + 2E_{12}^2} \quad (4)$$

¹Eq. (2) is actually obtained from the Mohr's circle for plane strain, which only applies under small strain assumption.

with:

$$E_{11} = \frac{F_{11}^2 + F_{21}^2 - 1}{2}, \quad (5a)$$

$$E_{12} = \frac{F_{11}F_{12} + F_{21}F_{22}}{2}, \quad (5b)$$

$$E_{22} = \frac{F_{12}^2 + F_{22}^2 - 1}{2}, \quad (5c)$$

$$E_{33} = \frac{(F_{11}F_{22} - F_{12}F_{21})^{-2} - 1}{2}. \quad (5d)$$

A generalization of ϵ_{IGP} to make it path-dependent is proposed in section 6.5.

3.2. CP constitutive laws

This subsection provides details about the fundamental equations used for CP simulations.

Let σ be the Cauchy's stress tensor. The resolved shear stress along the SS α is:

$$\tau^{(\alpha)} = \mathcal{S}^{(\alpha)} : \sigma \quad (6)$$

Here, ":" denotes the tensor product, contracted two times. $\mathcal{S}^{(\alpha)}$ is the Schmid tensor for SS α , such that its components are:

$$S_{ij}^{(\alpha)} = b_i^{(\alpha)} n_j^{(\alpha)} \quad (7)$$

In (7), $b_i^{(\alpha)}$ is the i -th component of slip direction and $n_j^{(\alpha)}$ is the j -th component of slip plane normal. Since the SSs are orientated here, plastic activity occurs on SS α if, and only if, $\tau^{(\alpha)}$ is greater than the corresponding CRSS, denoted $s^{(\alpha)}$ below. Let $\dot{\gamma}^{(\alpha)}$ be the shear rate on that SS. In this paper, we assume a rate-independent linear relationship between the time derivative of the CRSS of SS α (denoted $\dot{s}^{(\alpha)}$ below) and shear rates on all SSs. Face Centered Cubic (FCC) materials, like copper, have 24 oriented SSs²; thus we have (?):

$$\dot{s}^{(\alpha)} = \sum_{\beta=1}^{24} H_{\alpha\beta} \dot{\gamma}^{(\beta)}. \quad (8)$$

where $H_{\alpha\beta}$ denotes the components of the so-called hardening matrix. $H_{\alpha\alpha}$ is usually referred to as the self-hardening coefficient for SS α , whereas $H_{\alpha\beta}$ (with $\alpha \neq \beta$) is referred to as the latent-hardening coefficient on SS α because of

²If the SSs are oriented, we assume for instance that $[1\bar{1}0](111) \neq [\bar{1}10](111)$ and $\gamma^{(\alpha)} \geq 0$.

slip on system β . ? proposed the following evolution law:

$$H_{\alpha\beta} = \begin{cases} h_0 \left(1 - \frac{s^{(\beta)}}{s_\infty}\right)^a & \text{if } \mathbf{n}^{(\alpha)} = \mathbf{n}^{(\beta)}, \\ qh_0 \left(1 - \frac{s^{(\beta)}}{s_\infty}\right)^a & \text{otherwise.} \end{cases} \quad (9)$$

In (9), h_0 is the initial hardening rate, s_∞ is the saturation stress and a is a constant. q denotes the ratio of latent hardening rates to self hardening rates for non coplanar SSs, as first introduced by ?. Its value usually ranges between 1 to 2 (see ?, and references therein). The rate of plastic gradient is:

$$\mathbf{L}^P = \sum_{\alpha} \dot{\gamma}^{(\alpha)} \mathbf{S}^{(\alpha)}.$$

Thus, the plastic strain rate and spin tensors are:

$$\dot{\boldsymbol{\epsilon}}^P = \frac{1}{2} \left(\mathbf{L}^P + (\mathbf{L}^P)^{\top} \right), \quad (10a)$$

$$\dot{\boldsymbol{\omega}}^P = \frac{1}{2} \left(\mathbf{L}^P - (\mathbf{L}^P)^{\top} \right) \quad (10b)$$

respectively, where \top denotes the transpose operator. Under the small strain assumption, (10a) can be rewritten to get the plastic small strain tensor:

$$\boldsymbol{\epsilon}^P = \frac{1}{2} \sum_{\alpha} \gamma^{(\alpha)} \left[\mathbf{S}^{(\alpha)} + (\mathbf{S}^{(\alpha)})^{\top} \right] \quad (11)$$

where $\gamma^{(\alpha)}$ denotes the shear strain on SS α . Below, $\boldsymbol{\gamma}$ denotes the gathering vector for the values of the shear strain on each SS: $\boldsymbol{\gamma} = [\gamma^{(1)}, \gamma^{(2)}, \dots, \gamma^{(24)}]^{\top}$.

The ? model assumes that the strain is homogeneous within all the crystals and that no hardening occurs (all CRSSs remain constant). Thus, given the macroscopic plastic strain $\boldsymbol{\epsilon}^P$, the plastic shear strain on each SS $\gamma^{(\alpha)}$ is computed such that the straining energy is minimal and (11) holds; that is:

$$\boldsymbol{\gamma} = \underset{\mathbf{g} > 0}{\text{Arg min}} \left\{ \mathbf{s} \cdot \mathbf{g}, \text{ such that } \boldsymbol{\epsilon}^P = \frac{1}{2} \sum_{\alpha} g^{(\alpha)} \left[\mathbf{S}^{(\alpha)} + (\mathbf{S}^{(\alpha)})^{\top} \right] \right\}$$

where $\mathbf{g} = [g^{(1)}, g^{(2)}, \dots, g^{(24)}]^{\top}$ is the vector to be found, $\mathbf{s} = [s^{(1)}, s^{(2)}, \dots, s^{(24)}]^{\top}$ and “ \cdot ” stands for the dot product.

Conversely, the ? model assumes that the stress is homogeneous within all the crystals, and that the only SS undergoing plastic activity is the one with largest difference between its shear stress and its CRSS.

4. Identification of CP parameters through a Sachs model

This section proposes a numerical model, derived from that of ?, to estimate the macroscopic plastic behaviour of a polycrystalline aggregate. In its original paper, ? proposed to model the plastic behaviour of a polycrystal using the following assumptions:

- the stress is homogeneous within all crystals,
- only one SS is active at a time,
- this SS is determined by the largest difference between the shear stress and the CRSS,
- no hardening occurs.

Hence, the purpose of this section is to extend the Sachs model so that it takes into account strain hardening, interactions between SSs (8) and path-dependence of hardening parameters (9). In this model, we assume an homogeneous tensile stress along \mathbf{x} . Indeed, ? showed that, under this assumption, the Schmid factor alone was sufficient to find most of the slip traces.

4.1. The Sachs-based model

4.1.1. Single-crystal model (in small strain)

Consider a SS α with an initial shear strength $s_0^{(\alpha)}$. If the shear stress $\tau^{(\alpha)}$ on this SS is lower than $s_0^{(\alpha)}$, no slip is induced on α ($\gamma^{(\alpha)} = 0$). Conversely, if $\tau^{(\alpha)}$ exceeds $s_0^{(\alpha)}$, slip will occur ($\gamma^{(\alpha)} > 0$), inducing strain hardening, so that the updated shear strength will equal $\tau^{(\alpha)}$. Assuming the linear hardening law (8), it reads:

$$\tau^{(\alpha)} \leq s_0^{(\alpha)} \iff \gamma^{(\alpha)} = 0, \quad (12a)$$

$$\tau^{(\alpha)} = s_0^{(\alpha)} + \sum_{\beta} H_{\alpha\beta} \gamma^{(\beta)} \iff \gamma^{(\alpha)} > 0. \quad (12b)$$

As evidenced by (12b), we consider here that multiple slip can occur at once. Figure 4 schematically illustrates the influence of self and latent hardening on the evolution of CRSSs.

In the Sachs model, one wants to compute the strain on each SS α from the knowledge of σ ; that is assume the following:

- $\gamma^{(\alpha)} = 0$ for every α such that $\tau^{(\alpha)} \leq s_0^{(\alpha)}$ (case (b) in Figure 4),
- Solve (12b) for every other SSs (case (c) in Figure 4).

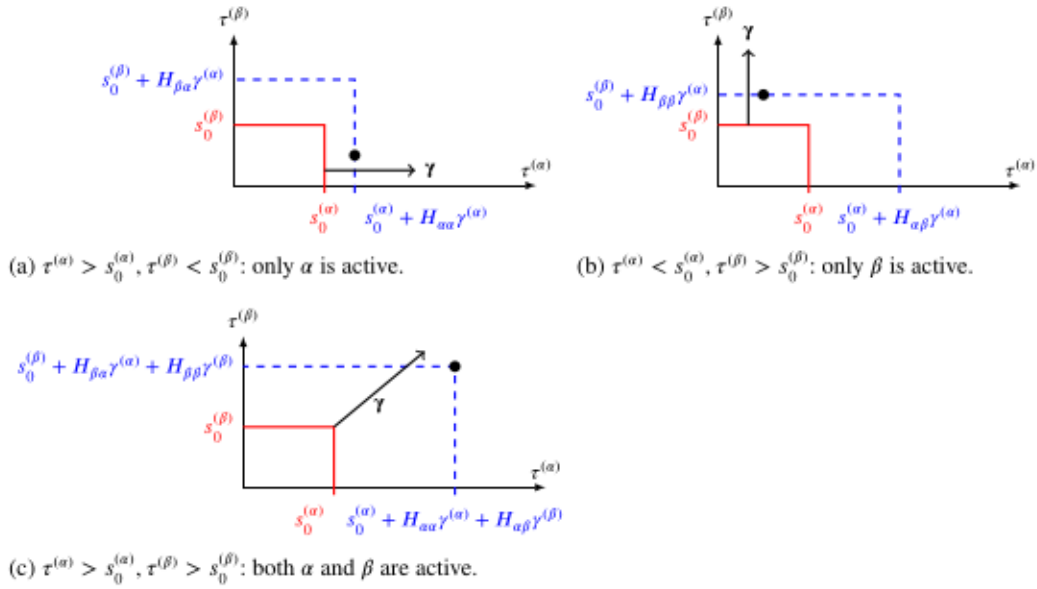


Figure 4: 2D representation of evolution of CRSSs in stress space, owing to (12): considering only two SSs α and β , this figure illustrates how their initial CRSSs (red) are updated (dashed blue), depending on the location of pair values of shear stresses in the stress space (black dot). Because of latent hardening, slip on SS α induces an increase of the CRSS on SS β (a) and vice-versa (b). Note that $\boldsymbol{\gamma}$ is intentionally not drawn parallel to the principal direction of expansion of yield surface, since $\boldsymbol{\gamma}$ is not necessarily an eigenvector of \mathbf{H} .

Let $\boldsymbol{\tau} = [\tau^{(1)}, \tau^{(2)}, \dots, \tau^{(24)}]^\top$ and $\mathbf{s}_0 = [s_0^{(1)}, s_0^{(2)}, \dots, s_0^{(24)}]^\top$. Now let $\tilde{\boldsymbol{\tau}}$ be the subset of $\boldsymbol{\tau}$ containing only components larger than shear strength. Utilizing the logical indexing notation³, this definition for $\tilde{\boldsymbol{\tau}}$ is simply:

$$\tilde{\boldsymbol{\tau}} = \boldsymbol{\tau} [\boldsymbol{\tau} > \mathbf{s}_0] .$$

Likewise, let:

$$\tilde{\boldsymbol{\gamma}} = \boldsymbol{\gamma} [\boldsymbol{\tau} > \mathbf{s}_0] ,$$

$$\tilde{\mathbf{s}}_0 = \mathbf{s}_0 [\boldsymbol{\tau} > \mathbf{s}_0] ,$$

$$\tilde{\mathbf{H}} = \mathbf{H} [\boldsymbol{\tau} > \mathbf{s}_0, \boldsymbol{\tau} > \mathbf{s}_0]$$

where \mathbf{H} is the hardening matrix introduced in (8). Thus, (12b) reads:

$$\tilde{\boldsymbol{\tau}} = \tilde{\mathbf{s}}_0 + \tilde{\mathbf{H}}\tilde{\boldsymbol{\gamma}} \quad \text{with } \tilde{\boldsymbol{\gamma}} > 0 \tag{13}$$

³Used for instance in MATLAB[®] or Python's array programming.

As a result, the resolution of the Sachs model with hardening consists in finding $\tilde{\boldsymbol{\gamma}}$ such that (13) is true. There is no exact solution for such condition, so an approximate solution is given by solving the corresponding Non-Negative Least Squares (NNLS) problem, as defined below:

$$\tilde{\boldsymbol{\gamma}} \approx \text{Arg min}_{\mathbf{p} > 0} \left\{ \|\tilde{\mathbf{H}}\mathbf{p} + \tilde{\mathbf{s}}_0 - \tilde{\boldsymbol{\tau}}\|_2^2 \right\} \quad (14)$$

where $\|\mathbf{a}\|_2$ denotes the euclidean norm of \mathbf{a} (i.e. $\|\mathbf{a}\|_2^2 = \mathbf{a}^\top \cdot \mathbf{a}$). Once (14) is solved, one can estimate the induced strain tensor using (11) whereas the small rotation tensor is:

$$\boldsymbol{\omega}^p = \frac{1}{2} \sum_{\alpha} \gamma^{(\alpha)} \left[\mathcal{S}^{(\alpha)} - (\mathcal{S}^{(\alpha)})^\top \right]$$

Algorithm 1 schematically sums up the proposed method to apply the Sachs model with linear hardening, under the small strain assumption, to a single crystal.

Algorithm 1 Single-crystal Sach model with linear hardening law: given the macroscopic stress $\boldsymbol{\sigma}$, the hardening matrix \mathbf{H} and the initial CRSSs \mathbf{s}_0 , this model returns the infinitesimal plastic strain tensor, the infinitesimal plastic rotation tensor and the updated CRSSs.

```

function SINGLECRYSTALMODEL( $\boldsymbol{\sigma}$ ,  $\mathbf{H}$ ,  $\mathbf{s}_0$ )
  for  $\alpha = 1..24$  do
     $\tau^{(\alpha)} \leftarrow \mathcal{S}^{(\alpha)} : \boldsymbol{\sigma}$  ▷ Shear stress on each SS
  end for
   $\tilde{\boldsymbol{\tau}} \leftarrow \boldsymbol{\tau}[\boldsymbol{\tau} > \mathbf{s}]$ 
   $\tilde{\mathbf{s}}_0 \leftarrow \mathbf{s}_0[\boldsymbol{\tau} > \mathbf{s}]$ 
   $\tilde{\mathbf{H}} \leftarrow \mathbf{H}[\boldsymbol{\tau} > \mathbf{s}, \boldsymbol{\tau} > \mathbf{s}]$ 
   $\tilde{\boldsymbol{\gamma}} \leftarrow \text{Arg min}_{\mathbf{p} > 0} \left\{ \|\tilde{\mathbf{H}}\mathbf{p} + \tilde{\mathbf{s}}_0 - \tilde{\boldsymbol{\tau}}\|_2^2 \right\}$  ▷ NNLS (14)
   $\boldsymbol{\gamma} \leftarrow \mathbf{0}$  ▷ Null default value for  $\gamma^\alpha$ 
   $\boldsymbol{\gamma}[\boldsymbol{\tau} > \mathbf{s}] \leftarrow \tilde{\boldsymbol{\gamma}}$  ▷ Retrieve non-zero values
   $\boldsymbol{\varepsilon}^p \leftarrow \sum_{\alpha} \frac{\gamma^{(\alpha)}}{2} \left[ \mathcal{S}^{(\alpha)} + (\mathcal{S}^{(\alpha)})^\top \right]$  ▷ Strain increment
   $\boldsymbol{\omega}^p \leftarrow \sum_{\alpha} \frac{\gamma^{(\alpha)}}{2} \left[ \mathcal{S}^{(\alpha)} - (\mathcal{S}^{(\alpha)})^\top \right]$  ▷ Rotation increment
   $\mathbf{s} \leftarrow \mathbf{H}\boldsymbol{\gamma} + \mathbf{s}_0$  ▷ Update CRSS
  return  $\boldsymbol{\varepsilon}^p$ ,  $\boldsymbol{\omega}^p$ ,  $\mathbf{s}$ 
end function

```

4.1.2. Polycrystalline model (in finite strain)

In this subsection, an integration scheme is proposed in the finite strain framework. To do so, time is discretized so that the small strain assumption applies between two subsequent time increments.

At first, consider a single crystal r whose orientation with respect to the reference Coordinate System (CS) is given by the rotation matrix \mathbf{g} . Let $\boldsymbol{\sigma}$ be the stress tensor, written in the reference CS. This tensor, written in the CS associated

to the crystal, becomes:

$$\sigma^* = \mathbf{g}^T \cdot \sigma \cdot \mathbf{g}$$

Now consider that the crystal undergoes finite strains. The backward Taylor's expansion of the plastic gradient F^P gives:

$$F^P(t - dt) = F^P(t) - \dot{F}^P dt$$

where \dot{F}^P denotes the material derivative of F^P and dt is the infinitesimal time increment. It reads (2, Chap. 5):

$$F^P(t - dt) = F^P(t) - L^P \cdot F^P(t) dt \quad (15)$$

$$= F^P(t) - (\dot{\epsilon}^P + \dot{\omega}^P) \cdot F^P(t) dt \quad (16)$$

$$= (\delta - d\epsilon^P - d\omega^P) \cdot F(t) \quad (17)$$

where δ is the 2nd order identity tensor, whereas $d\epsilon^P$ and $d\omega^P$ are the infinitesimal plastic strain and rotation increment tensors, respectively. Let $d\epsilon^{P*}$ and $d\omega^{P*}$ be the aforementioned tensors, but expressed in a CS associated to the crystal; in this case, (17) becomes:

$$F^P(t - dt) = [\delta - \mathbf{g} \cdot (d\epsilon^{P*} + d\omega^{P*}) \cdot \mathbf{g}^T] \cdot F^P(t)$$

As a result, a possible implicit integration scheme is:

$$F^P(t) = \delta F \cdot F^P(t - dt)$$

with

$$\delta F = \mathbf{g} \cdot [\delta - d\epsilon^{P*} - d\omega^{P*}]^{-1} \cdot \mathbf{g}^T$$

After straining, the orientation of the crystal becomes (2, Chap. 2):

$$\mathbf{g}(t + dt) = \mathbf{g}(t) \cdot \exp(d\omega^{P*}) \quad (18)$$

where \exp denotes the matrix exponential operator⁴. Eq. (18) holds if:

$$(\mathbf{d}\boldsymbol{\omega}^{\text{P}^*})^\top : \mathbf{d}\boldsymbol{\omega}^{\text{P}^*} < 2\pi^2. \quad (19)$$

Considering a bulk material as a set of crystals, we assume that the macroscopic plastic gradient $\overline{\mathbf{F}^{\text{P}}}$ is the arithmetic mean value of the plastic gradients of each crystal (?, Chap. 8). The macroscopic plastic right Cauchy-Green (rCG) tensor is:

$$\overline{\mathbf{C}^{\text{P}}} = \left(\overline{\mathbf{F}^{\text{P}}}\right)^\top \cdot \overline{\mathbf{F}^{\text{P}}}.$$

Thus, the elongation along the \mathbf{x} direction because of plastic deformation can be estimated as follows (?, Chap. 2):

$$\epsilon_{11}^{\text{P}} = \sqrt{\overline{\mathbf{C}^{\text{P}}}_{11}} - 1.$$

In the proposed model (called Sachs hereafter), we assume that the elastic strain is small ($< 2 \times 10^{-3}$), so that the total elongation along \mathbf{x} direction is just:

$$\epsilon_{11} \approx \epsilon_{11}^{\text{P}} + \epsilon_{11}^{\text{e}} \quad (20)$$

where ϵ_{11}^{e} denotes the elastic stretch of the bulk along \mathbf{x} , computed from the Hill average (see Appendix A for details). Note that for larger elastic strain, the Hooke's law (37) and the additive assumption (20) do not apply. In this case, one should use the second Piola–Kirchhoff stress tensor (?) or the corotational Jaumann stress rate tensor (??) to compute the elastic gradient.

An incremental scheme, taking into account all the equations detailed below can now be set up, taking advantage of the single-crystal Sachs model proposed in section 4.1.1 at each increment. The hardening matrix of each crystal is updated with respect to the power law (9) at each increment. This scheme is valid as long as the step sizes dt are small enough so that the small strain assumption is true within each step:

$$\|\mathbf{d}\boldsymbol{\epsilon}\|_\infty \ll 1 \quad (21)$$

and (19) applies. In (21), $\|\cdot\|_\infty$ denotes the infinity norm. Algorithm 2 illustrates an implementation of the proposed method to simulate a stress-controlled tensile test applied on a polycrystal.

⁴So that $\exp(\mathbf{A}) = \sum_{k=0}^{\infty} \frac{1}{k!} \mathbf{A}^k$.

Algorithm 2 Incremental polycrystalline Sach model with linear hardening law, taking into account the elastic strain. n_C denotes the number of considered crystals (1000 in this work).

```

for all  $r = 1 \dots n_C$  do
   $F^{p(r)} \leftarrow \delta$  ▷ Initialize the plastic gradient tensor of each crystal
   $\mathbf{g}^{(r)} \leftarrow$  Random orientation from texture
   $\mathbf{H}^{(r)} \leftarrow$  Initial hardening matrix
   $\mathbf{s}^{(r)} \leftarrow s_0$  Initial shear strengths
end for
for all Time step  $t$  do
  for  $r=1 \dots n_C$  do
     $\sigma^{*(r)} \leftarrow (\mathbf{g}^{(r)})^\top \cdot \boldsymbol{\sigma}(t) \cdot \mathbf{g}^{(r)}$  ▷ Current stress tensor in crystal CS
     $d\boldsymbol{\varepsilon}^p, d\boldsymbol{\omega}^p, \mathbf{s}^{(r)} \leftarrow \text{SINGLECRYSTALMODEL}(\sigma^{*(r)}, \mathbf{H}^{(r)}, \mathbf{s}^{(r)})$  ▷ Algo. 1.
     $\delta F \leftarrow \mathbf{g}^{(r)} \cdot [\delta - d\boldsymbol{\varepsilon}^p - d\boldsymbol{\omega}^p]^{-1} \cdot (\mathbf{g}^{(r)})^\top$  ▷ Gradient increment (in reference CS)
     $F^{p(r)} \leftarrow \delta F \cdot F^{p(r)}$  ▷ Update the plastic gradient of crystal ( $r$ )
     $\mathbf{g}^{(r)} \leftarrow \mathbf{g}^{(r)} \cdot \exp(d\boldsymbol{\omega}^{(r)})$  ▷ Update the crystal orientation
    for  $\alpha, \beta=1 \dots 24$  do
       $H_{\alpha\beta}^{(r)} \leftarrow [q]h_0 \left(1 - \frac{s^{(r,\beta)}}{s_\infty}\right)^a$  ▷ update hardening matrix (9)
    end for
  end for
   $\overline{F^p} \leftarrow \frac{1}{n_C} \sum_r F^{p(r)}$  ▷ Mean plastic gradient
   $\overline{C^p} = \left(\overline{F^p}\right)^\top \cdot \overline{F^p}$  ▷ Macroscopic right C.-G. tensor
   $c_H \leftarrow \text{HILL}(c, \{\mathbf{g}^{(1)}, \mathbf{g}^{(2)}, \dots, \mathbf{g}^{(n_C)}\})$  ▷ Hill average (38)
   $\boldsymbol{\varepsilon}^e \leftarrow c_H^{-1} : \boldsymbol{\sigma}(t)$  ▷ Mean elastic strain
   $\varepsilon_{11}(t) \leftarrow \sqrt{\overline{C^p}_{11}} - 1 + \varepsilon_{11}^e$  ▷ Total elongation along  $\mathbf{x}$ 
end for

```

4.2. Inverse analysis

The incremental polycrystalline model proposed in Algorithm 2 was used to estimate the parameters q , s_0 , H_0 , a and s_∞ from the experimental tensile curve through an inverse analysis scheme. This optimization consisted in minimizing the cost function:

$$\chi^{\text{Sachs}} = \sum_i \left(\varepsilon_{11}^i - \varepsilon_{\text{expe}}^i \right)^2 \quad (22)$$

where ε_{11}^i (resp. $\varepsilon_{\text{expe}}^i$) denotes the simulated elongation (resp. experimental elongation) measured at date i . The search interval for q was $[1, 2]$ (?), whereas these for the other parameters were arbitrary set to the values given in Table 1. The simulations were done with 300 times steps and 1000 unique orientations, randomly picked from the experimental ones (EBSD data). These numbers of time steps and orientations were set by trial and error, leading to the best compromise between reproducibility and computational time. The trust-region algorithm (?) was used to minimize χ^{Sachs} . The optimization task took about 10 hours to complete on a 8-core Intel® Core™ i9-9880H CPU @ 2.30 GHz. The elastic properties of copper were provided by ?. Table 1 gives the results of this inverse analysis. As a comparison, the values

Table 1

Results from inverse analysis using the Sachs model (Algo. 2).

	q	h_0 MPa	s_0 MPa	s_{∞} MPa	a
Search interval	[1, 2]	[100, 700]	[5, 20]	[100, 200]	[2, 4]
Initial guess ^a	1.4	180	16	148	2.25
Sachs model	1.775	401.2	18.52	160	2.351

^a Taken from ?.

used by ? (and latter by ?) are also given in this table. It is clear that the main difference is for the initial hardening coefficient, which is more than twice larger than that used by ?. This discrepancy may be related to different chemical compositions between the two materials or different grain size distributions (?). Figure 2 illustrates the results of the Sachs-based inverse analysis in terms of macroscopic tensile behaviour (orange solid line). This curve can be compared against the experimental tensile curve (blue dotted line), evidencing a very good fit between the model and the experiment. Nevertheless, it is worth mentioning that the onset of plastic deformation (when $\sigma < 50$ MPa) is not accurately modelled. This can be related to the relatively large value for h_0 , as mentioned above. At this stage of the analysis, the initial guess used for optimization was taken from ?. The influence of this initial guess is further discussed in section 6.1.

In order to evidence the changes in crystallographic texture between the initial and the deformed microstructures, the Orientation Distribution Functions (ODFs) at the initial stage and at the end of loading (step 3 in Figure 2) were computed with MTEX (?) from all the 1000 aforementioned orientations. In order to analyse these changes independently of the initial texture, the changes in ODF were computed:

$$\Delta\text{ODF} = \text{ODF}(\text{step 3}) - \text{ODF}(\text{initial}) . \quad (23)$$

As a result, the values of ΔODF given by the Sachs model is illustrated as Pole Figures (PFs) in Figure 5a. As a comparison, the experimental values of ΔODF , measured from EBSD data, are illustrated in Figure 5b. It is thus clear that the simulated texture is similar to the experimental one, evidencing a near transverse isotropy perpendicular to the tensile direction ($y - z$ plane), with an alignment of $\{111\}$ and a $\{110\}$ antipole (negative change) with the tensile direction. This is in agreement with the typical texture evolution of FCC metals undergoing uniaxial tensile strain (e.g. ?). However, the intensity of these changes seems overestimated in the simulation, compared to the experiment. The sharpness of the crystallographic texture is usually characterized through the Texture Index (TI), defined here as:

$$\text{TI} = \oint_{\mathcal{E}} [\Delta\text{ODF}(\mathbf{g})]^2 d\mathbf{g} \quad (24)$$

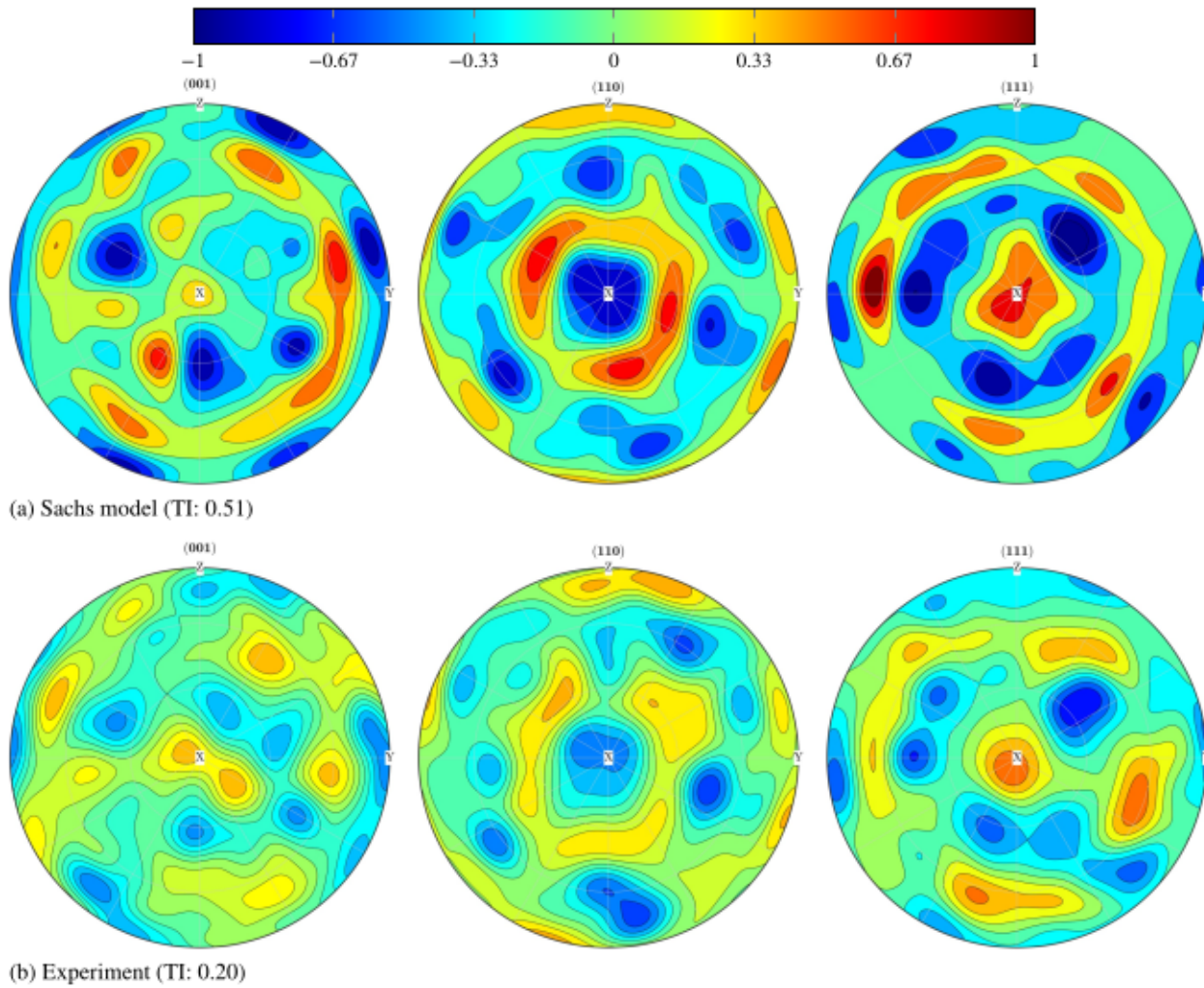


Figure 5: Pole Figures illustrating the changes in ODF between the initial and the final crystallographic texture. The tensile direction is out-of-plane.

where \mathcal{E} denotes the Euler space. Hence, the TI was 0.51 in the simulation, whereas it was 0.20 in the experiment. This suggests that the changes in crystallographic orientations are overestimated by the Sachs model, compared to the experimental results.

5. CPFEM-based inverse analysis from full-field measurements

In this section, the inverse analysis used by comparison between the CPFEM results and the experimental data (DIC measurements and tensile curve) is detailed.

The estimator for CP parameters found using the Sachs model was used as an initial guess for another inverse analysis. Thus, this section provides details about this second inverse analysis, which is based on CPFEM and use data from full-field measurements. First, the methods used for CPFEM is given, then the cost functions used for inverse

analysis are detailed. Secondly, a scheme for minimizing these cost functions is proposed. Finally, the results from CPFEM are presented.

5.1. CPFEM model

CPFEM simulations were run using the PRISMS-Plasticity software (?). The same constitutive laws as in the Sachs model (see sec. 3.2) were used for these simulations⁵. A mesh conforming the grain shapes was generated beforehand from EBSD data thanks to the MTEX2Gmsh toolbox for MATLAB® (?). The full procedure for generating input data for PRISMS-Plasticity from EBSD is detailed elsewhere⁶. The typical element size at GBs was 2 μm, with an increasing element size with increasing distance from the GBs. As a result, the mesh consisted in 30 366 nodes and 14 897 hexahedron elements with one element in thickness, as represented in Figure 6. DICBCs were prescribed at the

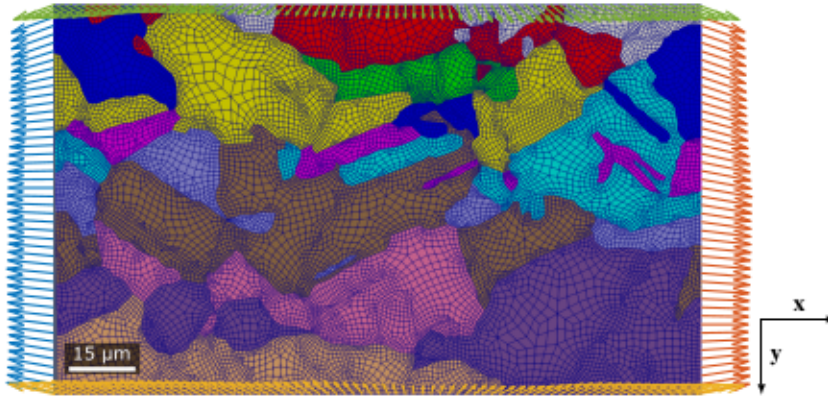


Figure 6: Mesh obtained from the reconstructed grains (see Fig. 1) using MTEX2Gmsh (?): the colour relates to the grain ID. Arrows at the borders illustrate the applied BCs at step 3 (true scale). The size of the mesh was $151 \times 91 \times 2 \mu\text{m}^3$ ($x \times y \times z$).

outer surface of the mesh (i.e. that corresponding to the RoI in the $x - y$ plane) with the aid the SEM-DIC pipeline for PRISMS-Plasticity (?). Coloured arrows in Figure 6 represent the DICBCs at step 3. The front and back surfaces of the mesh in Figure 6 were considered stress-free, leading to near plane-stress condition in $x - y$ plane.

5.2. Cost functions

Let $\mathbf{u}_i^{\text{FEM}}(t_j)$ be the displacement given at node i and time step t_j by CPFEM. Likewise, let $\mathbf{u}_i^{\text{DIC}}(t_j)$ be the corresponding displacement measured by DIC. The displacement error function is defined as:

$$\delta \mathbf{u}_{i,j} = \mathbf{u}_i^{\text{FEM}}(t_j) - \mathbf{u}_i^{\text{DIC}}(t_j). \quad (25)$$

⁵Except the fact that finite elastic strain was considered in this case, as opposed to (20). See (?) for details.

⁶<https://github.com/DorianDepriester/MTEX2Gmsh/blob/master/MTEX2prisms/MTEX2PRISMS.pdf>

The kinematic cost function can be defined as follows:

$$\chi^u = \frac{1}{n_{\text{step}}} \sum_{j=1}^{n_{\text{step}}} \sum_{i=1}^n \langle \delta \mathbf{u} \rangle_{i,j}$$

where $\langle \delta \mathbf{u} \rangle_{i,j}$ is the normalized displacement error, such that:

$$\langle \delta \mathbf{u} \rangle_{i,j} = \frac{1}{K_j^u} \frac{\|\delta \mathbf{u}_{i,j}\|_2^2}{\text{Corr}_{i,j}}. \quad (26)$$

In (26), $\text{Corr}_{i,j}$ denotes the correlation coefficient at pixel i and time step t_j and

$$K_j^u = \sum_{i=1}^n \frac{\|\mathbf{u}_i^{\text{DIC}}(t_j)\|_2^2}{\text{Corr}_{i,j}}. \quad (27)$$

In (26) and (27), denominator $\text{Corr}_{i,j}$ helps neglecting values where the correlation is poor ($\text{Corr} \gg 0$), compared to other locations where the correlation is good ($\text{Corr} \sim 0$). The K_j^u denominator stands for normalizing the cost function (dimensionless). For instance, we have $\chi^u = 1 \times 10^{-2}$ if $\mathbf{u}^{\text{FEM}} = 1.1\mathbf{u}^{\text{DIC}}$ everywhere. In this work, DIC measurements were made at the same locations as mesh nodes. In case of inconsistent locations, a procedure to map (project) the displacements given at DIC locations to mesh nodes is proposed in appendix B.

Let σ_j^{exp} be the macroscopic stress experimentally measured at time step t_j . Likewise, let $\langle \sigma_{xx}^{\text{FEM}} \rangle_j$ be the macroscopic tensile stress along \mathbf{x} direction, computed by FEM at time step t_j . Thus, the cost function on the tensile curve can be defined as follows:

$$\chi^\sigma = \frac{1}{K^\sigma} \sum_{j=1}^{n_{\text{inc}}} \left(\langle \sigma_{xx}^{\text{FEM}} \rangle_j - \sigma_j^{\text{exp}} \right)^2 \quad (28)$$

with

$$K^\sigma = \sum_{j=1}^{n_{\text{inc}}} \left(\sigma_j^{\text{exp}} \right)^2. \quad (29)$$

Again, χ^σ is dimensionless here, so that $\chi^\sigma = 1 \times 10^{-2}$ if $\langle \sigma_{xx}^{\text{FEM}} \rangle = 1.1\sigma^{\text{exp}}$ for all increments.

As a result, the overall cost function can be defined as the weighted average of χ^u and χ^σ (?):

$$\chi = (1 - \omega^\sigma) \chi^u + \omega^\sigma \chi^\sigma. \quad (30)$$

In this work, we used $\omega^\sigma = 0.5$ (balanced weights between kinematic and tensile responses, as suggested by ? and ?).

5.3. Optimization algorithm

The Limited-memory Broyden–Fletcher–Goldfarb–Shanno algorithm with Box constraints (L-BFGS-B) (?) was used to minimize the cost function (30) with the same bounds as in the Sachs-based inverse analysis (see Table 1). Indeed, this minimizing technique was proved to be efficient for inverse analysis involving FEM simulations (?). At each iteration, L-BFGS-B estimates the cost function for $n + 1$ parameter values (where n denotes the number of parameters to estimate, 5 here). These $n + 1$ evaluations are then used to compute the gradient around a particular value for the parameters. Thus, a parallel implementation of L-BFGS-B (?) was used to run multiple evaluations at once. Figure 7 illustrates the implementation of the optimization algorithm. All the source code used for performing

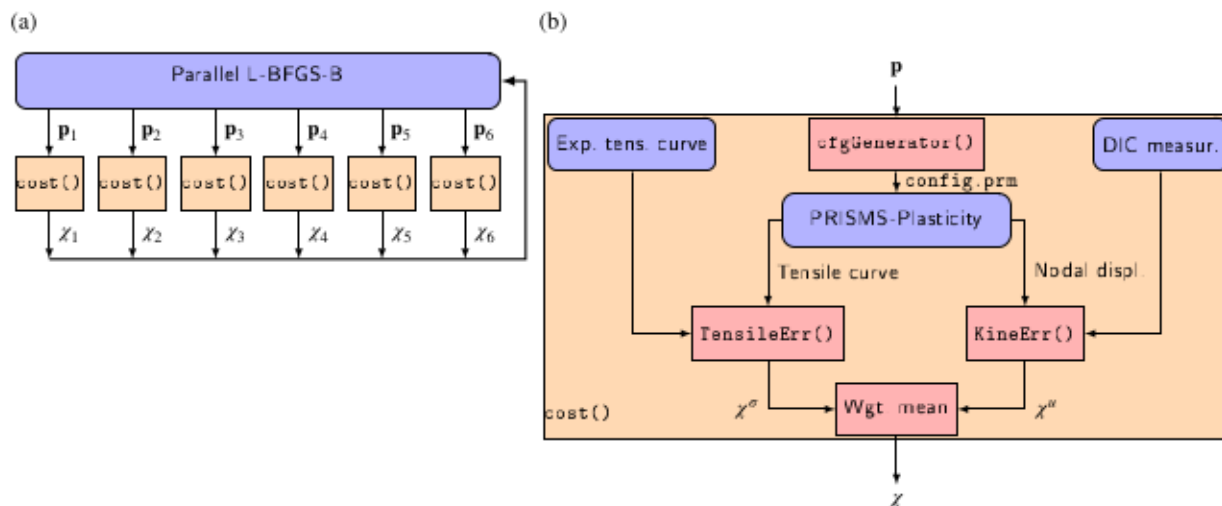


Figure 7: Schematic representation of the optimization algorithm: (a) at each iteration, 6 evaluations of the `cost()` function are made in parallel, depending on the parameters $\mathbf{p} = (q, h_0, s_0, s_\infty, a)$. Figure (b) provides details about how the `cost()` function is computed. Each call of `cost()` generates an input file for PRISMS-Plasticity (`config.prm`) from \mathbf{p} through `cfgGenerator()` then run the simulation.

this optimization is freely available online⁷.

The optimization was run on the MSMP's High Performance Computing (HPC) cluster, using 8 CPU cores for each simulation. These simulations lasted 50 to 100 hours each, depending on the simulation parameters and the cluster's node. The optimization algorithm was stopped at the 13th iteration, that is after 78 CPFEM simulations. The whole optimization task lasted about 1300 hours (55 days).

5.4. Results

5.4.1. Optimization

The parameters identified by CPFEM-based inverse analysis are given in Table 2. The corresponding macroscopic tensile curve obtained by CPFEM is depicted in Figure 2 (red dashed line). It is clear that the correlation is good with

⁷<https://github.com/DorianDepriester/OptiPRISMS>

Table 2

Results from optimization made by CPFEM.

Optimization stage	q	h_0 MPa	s_0 MPa	s_∞ MPa	a	χ
Initial guess ^a	1.775	401.2	18.52	160.0	2.351	9.066×10^{-2}
End	1.702	309.5	12.22	121.8	2.192	1.063×10^{-2}

^a Taken from the Sachs-based optimization (see Table 1)

the experimental results (blue dots) in the investigated range of strain (0 to 0.12). Figure 8 shows the normalized displacement error $\langle \delta \mathbf{u} \rangle_{i,j}$, as defined in (26), at each step. It appears that the correlation is good between DIC

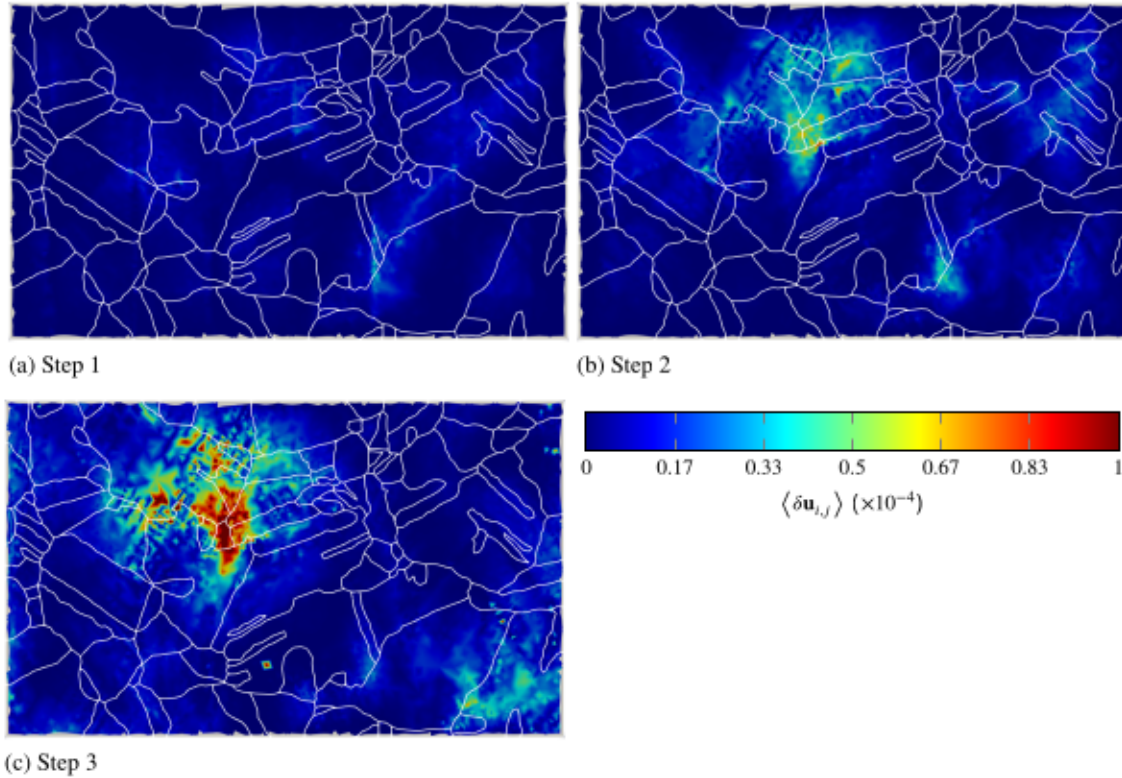


Figure 8: Normalized displacement errors (26) between DIC and CPFEM. White lines represent the grain boundaries.

measurements and displacement given by CPFEM, although a region shows poor consistency at steps 2 and 3. Considering the size and the shape of this region, this poor correlation may be due to grains beneath the surface which locally drive the mechanical behaviour, perhaps because the thickness of the apparent grains in this region is very small. As a reminder, grains were supposed columnar along \mathbf{z} , and one element in thickness was used here (near plane-stress assumption). Further analyses, involving thin-layer removal, like Focused Ion Beam (FIB), should be performed to reveal the microstructure underneath. Note that the displacement error function was not computed on boundaries, for it was necessarily 0 because of DICBCs.

In Figure 2, the green dotted line illustrates the tensile curve from CPFEM at the beginning of optimization (that is, using the CP parameters given by the Sachs-based inverse analysis). In this case, the CPFEM simulation overestimates the tensile stress by about 15 MPa, hence the need for this second optimization stage. Figure 9 illustrates the evolution of the cost function and the CP parameters depending on the L-BFGS-B iteration step. It is thus clear that L-BFGS-B

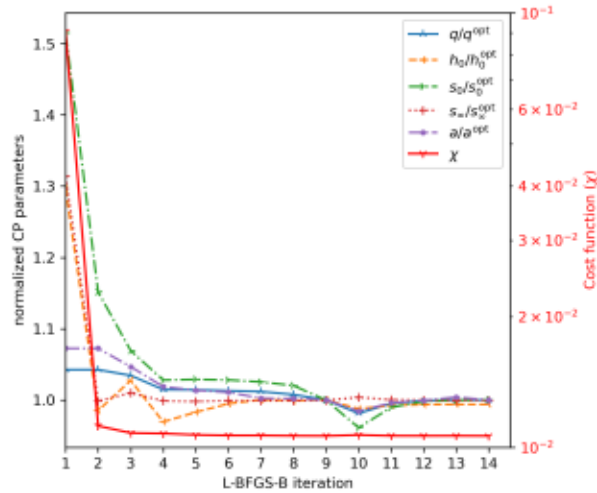


Figure 9: Evolution of the CP parameters and of the cost function (χ), depending on the iteration step of optimization loops. For the sake of clarity, each CP parameter was normalized with respect to the optimal one, as given in Table 2.

quickly converges toward the final values, both in terms of cost function (χ) and CP parameters (q , h_0 , s_0 , s_∞ and a), and it can be concluded that convergence is reached after 6 iterations (i.e. after about 600 h of computing), even though the L-BFGS-B stopping criterion was not reached. However, it is worth noting that s_0 converges slowly, compared to other parameters. This suggests that this parameter is harder to estimate correctly by the proposed approach. This can be due to the large value of h_0 , which lead to rapid increase of the yield stress at the early stages of plastic strain. The fact that χ does not converge toward 0 is probably due to the low-correlation region mentioned above, where optimization loops fail to replicate the displacement. Other authors (e.g. ??) faced the same issue (non-decreasing cost function), but ? attributed this to local minima whereas ? assumed this was due to an inappropriate constitutive law.

5.4.2. CPFEM simulations

Figure 10 shows the result of CPFEM in terms of equivalent strain at each experimental step (as defined in Figure 2). It appears that localization occurs even at macroscopic strain as low as 0.04 (step 2), but the strain distribution appears even more inhomogeneous at further step (Step 3). This is in accordance with ?. At steps 2 and 3, the strain distribution is heterogeneous between grains, but also within each grain. This suggests that the strain is not only related to the orientation of the grains, but also to their neighbours. It is clear that the localization bands, as reported by ?, are not modelled. Other simulations using a very fine mesh (with element size around 50 nm) confirmed that the CP constitutive

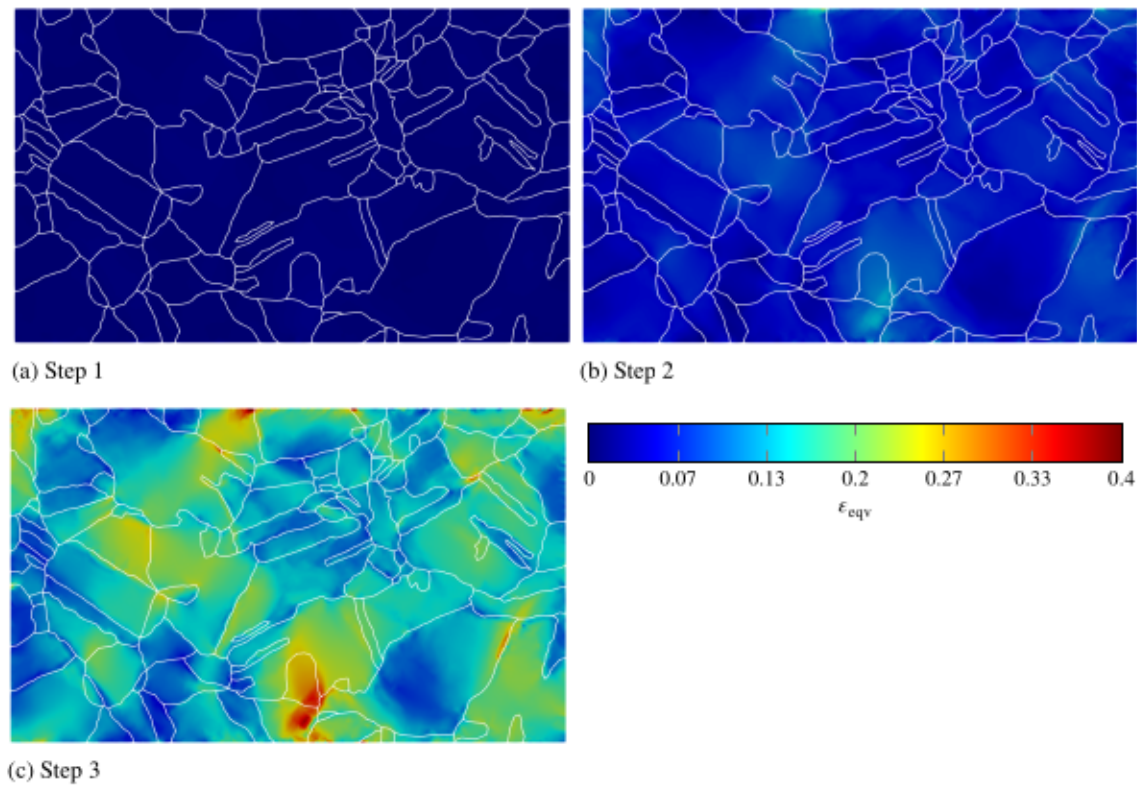


Figure 10: Equivalent strain given by CPFEM. White lines represent the grain boundaries.

laws used here were not able to predict localization bands. When compared to DIC measurements (as shown in Fig. 3b), it appears that the strain localization is well modelled at grain scale, but the intragranular spread is rather different. This may be due to intragranular misorientations which are not taken into account in CPFEM (each grain is assumed to have uniform initial orientation, hence no intragranular misorientation) or because of interaction with sub-surfaced grains (?).

In order to assess the present results, Figure 11 illustrates the local values of equivalent strain, experimentally measured by DIC with $\varphi = 9.6 \mu\text{m}$ (see Fig. 3b), as a function of the corresponding equivalent strain estimated by CPFEM. The overall trend is adequate ($R^2 = 0.724$), but the spread evidences discrepancies between DIC and CPFEM at local scale. On average, the simulated equivalent strain is 9% larger than that measured by DIC. The possible culprits for these discrepancies are discussed in section 6.4. Because of the aforementioned disparities, performing inverse analysis from strain measurements — as ? did — can possibly lead to large errors. It is worth mentioning that the relevance of the criteria used here (ϵ_{IGP} and ϵ_{eqv}) are further investigated in section 6.4.

Figure 12 illustrates the von Mises equivalent stress at each step. The distribution of equivalent stress is rather different from that of equivalent strain. Indeed, it seems that stress localization mainly occurs near GBs, probably because of strain incompatibilities. This is consistent with the stress concentration reported on other metallic alloys,

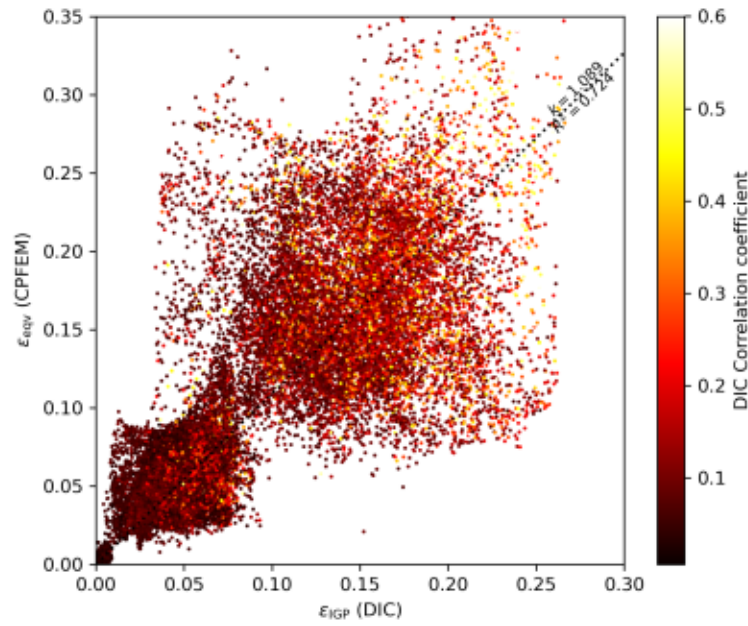


Figure 11: Equivalent strain (ϵ_{eqv}) simulated by CPFEM as a function of the experimental values (ϵ_{IGP}) given by DIC. Each dot is coloured depending on the correlation coefficient. The dotted line illustrates the results from linear regression.

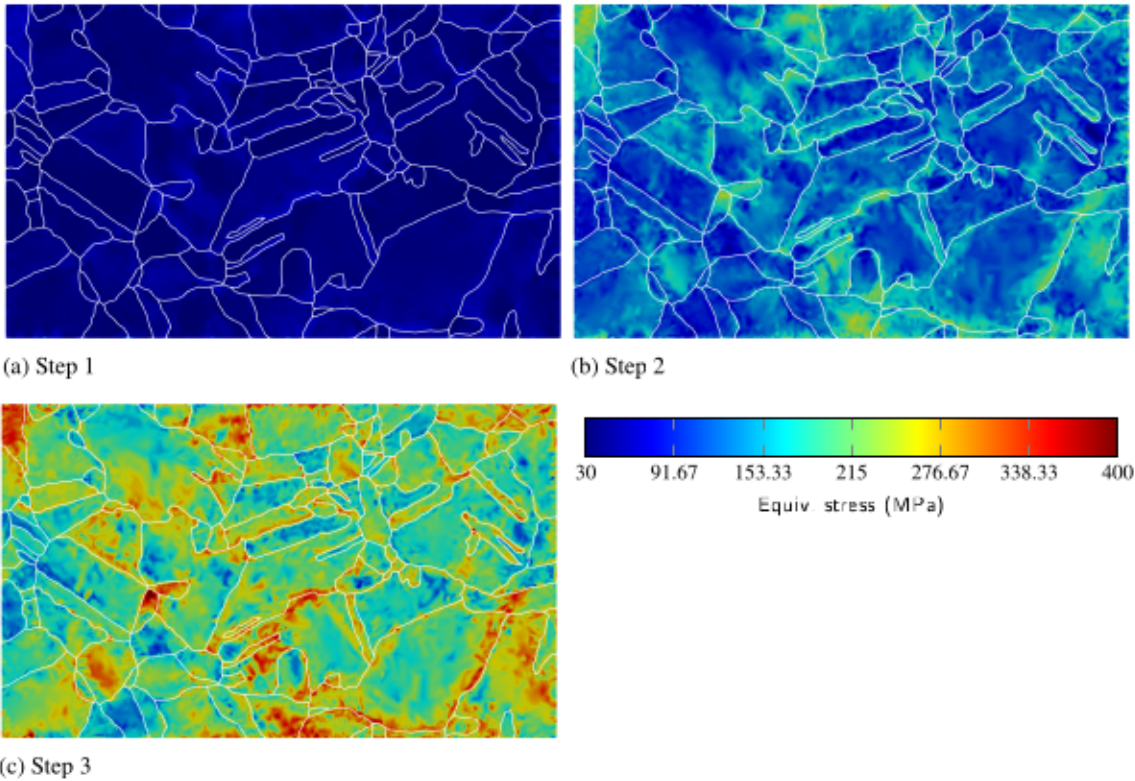


Figure 12: Equivalent stress given by CPFEM.

such as Al7075 (?) or SAC305 (?). Conversely, on average, the stress seems somehow homogeneously distributed between grains. This is in accordance with the analysis performed by DIC (?). To check this statement, Figure 13 illustrates the tensile stress along the x axis. Thus, it is clear that this hypothesis is rather true at early stages of the

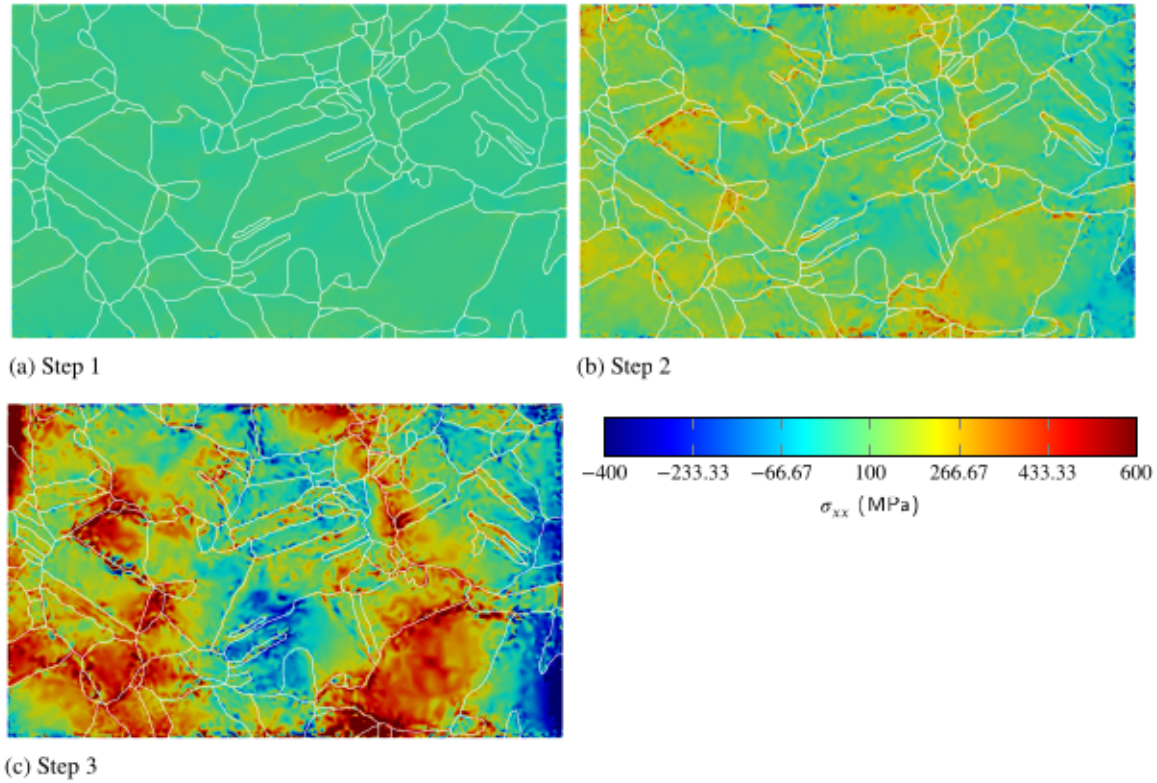


Figure 13: Tensile stress along X direction given by CPFEM.

deformation (steps 1 and 2), but becomes untrue at larger strain (step 3). Indeed, in this case, the tensile stress is clearly heterogeneous between grains and within each grain. Some regions even undergo compressive stress. This breaks the fundamental hypothesis of the Sachs model (uniform stress over all grains); thus, this may explain the discrepancy between the experimental evolution of crystallographic texture and that simulated with the Sachs model (see section 4.2).

The evolution of crystallographic texture, computed from CPFEM simulation, can be investigated in terms of ODF changes. Figure 14 illustrates the PFs from Δ ODF, as defined in (23), computed from CPFEM results. It appears that the corresponding PFs display similar patterns than experimental ones (see Fig. 5b), namely: a $\{110\}$ antipole and an alignment of $\{111\}$ near x direction, and a ring-like $\{111\}$ distribution tilted by 60° from x . The texture sharpness is weaker here ($TI = 0.23$) than in the Sachs model (see Fig. 5a). However, the texture evolutions appears orthotropic, with missing (110) poles in the $x - y$ plane. This discrepancy may be because the CPFEM simulations were made assuming a constant orientation within each grain (the mean orientation of each grain was used), whereas random

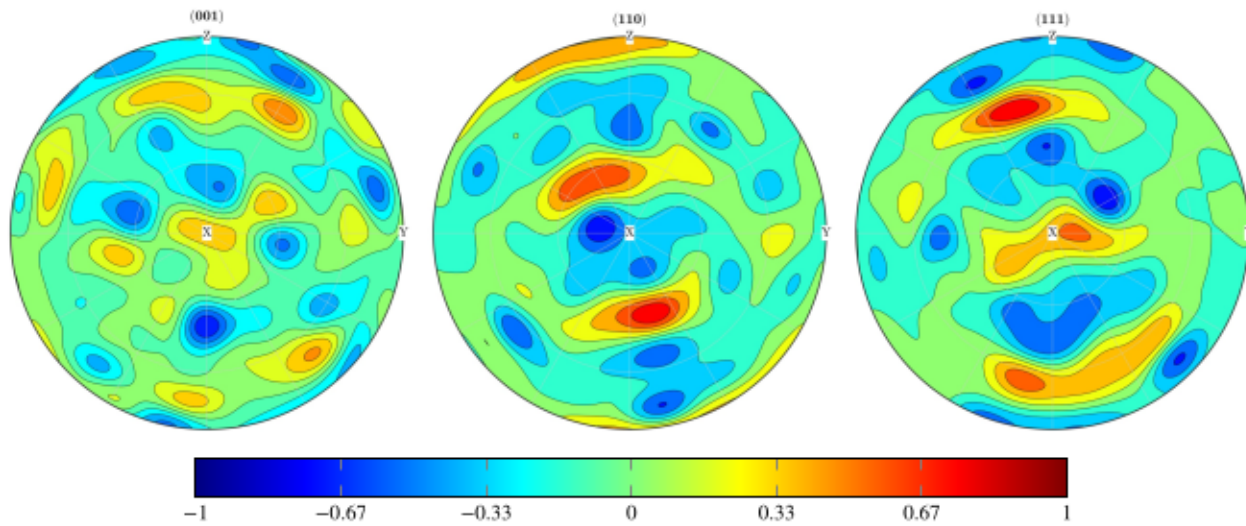


Figure 14: PFs reconstructed from the change in texture (ΔODF), given by CPFEM simulations (TI: 0.23).

orientations from EBSD data were used in the Sachs model. This suggests that the number of reconstructed grains (115 here) is not large enough for representativeness of the whole orientations. This disagrees with the fact that 50 grains are enough when experimentally investigating the texture evolution, as reported by ?. This discrepancy may be related to the interaction with grain outside the meshed volume (outside the RoI or beneath the surface imaged by EBSD).

6. Discussion

6.1. Influence of the initial guess in Sachs inverse analysis

In this subsection, the influence of the initial guess for the Sachs-based inverse analysis is studied.

In the Sachs-based inverse analysis (detailed in sec. 4.2), the initial guesses for q , h_0 , s_0 , s_∞ and a were taken from ?. Although inverse analysis is now commonly performed for CP simulations, the robustness of such approach against local minima and the uniqueness of the solution are rarely discussed in literature (???). Thus, the Sachs-based optimization was run through a multistart scheme, with 8 initial guesses randomly picked from the investigated space (see intervals in Table 1). Results from this multistart optimization are summed up in Table 3. Depending on the initial guess, the minimizer converges toward different values. For instance, the optimization task #6 has failed; analysis of this case showed that the initial CP values actually lead to unrealistic results (with $\epsilon_{11} > 1$). This table also evidences local minima of the cost function χ^{Sachs} (22). Indeed, considering the final values of χ^{Sachs} , only the optimized parameters given in rows #0, #1, #4 and #7 and #8 can be considered as global minimizers (see bold values in Table 3). The Coefficient of Variations⁸ (CoV) were computed from these selected values, as given in Table 3. As a result, it appears

⁸Ratio of the standard deviation to the mean.

Table 3

Results from multistart optimization made from the Sachs model. The row #0 corresponds to the optimization made in section 4.2. Bold values highlights where $\chi^{\text{Sachs}} < 1 \times 10^{-4}$.

	Initial guess					Optimized value					
	q	h_0	s_0	s_∞	a	q	h_0	s_0	s_∞	a	χ^{Sachs}
#0	1.4	180	16	148	2.25	1.775	401.2	18.52	160	2.351	2.63×10^{-5}
#1	1.17	635	9.26	183.6	3.11	1.306	431.0	18.55	186.94	3.01	3.43×10^{-5}
#2	1.85	220	15.4	164.9	3.17	1.902	402.1	17.53	176.48	2.78	6.37×10^{-4}
#3	1.64	372	5.02	162.1	3.02	1.764	418.42	10.02	171.89	2.76	3.14×10^{-3}
#4	1.00	309	14.5	161.8	2.47	1.236	415.23	18.80	162.85	2.41	4.02×10^{-5}
#5	1.66	328	6.45	189.7	3.73	1.761	423.92	10.01	192.62	3.22	3.02×10^{-3}
#6	1.40	260	7.44	111.7	3.12	1.407	259.15	7.418	113.61	3.09	19.649
#7	1.34	355	8.08	111.6	2.54	1.490	433.71	17.92	155.28	2.44	5.63×10^{-5}
#8	1.06	424	5.04	174.0	3.56	1.327	434.97	18.41	191.21	3.12	3.52×10^{-5}
CoV ^a						0.15	0.035	0.018	0.097	0.13	

^a Computed from bold values

that the Sachs-based optimization is robust for finding h_0 , s_0 and s_∞ . Conversely, it leads to larger uncertainty on q and a (CoV > 0.1). However, the optimization fails if the initial guess is too far from realistic values. ? also showed that, when using a cost function based on load-displacement curve in nano-indentation, CPFEM-based inverse analysis is robust for finding h_0 , s_0 and s_∞ .

The tensile curves, computed with the Sachs model and using the aforementioned selected values for the CP parameters, are illustrated in Figure 15. It is clear that the tensile curves are barely distinguishable. This indicates the non-uniqueness of the solution, as stated by ?, ?, and ?. It is worth noticing that all the selected values in Table 3

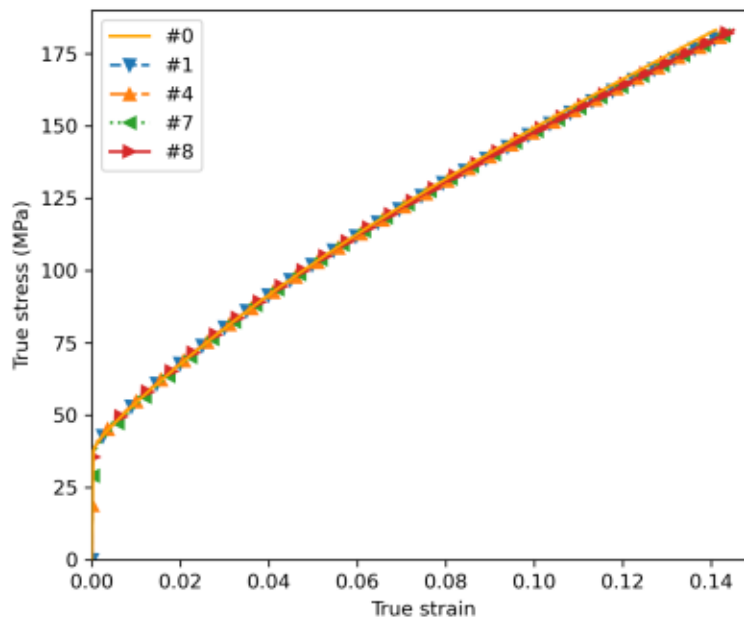


Figure 15: Sachs model: tensile curves corresponding to the selected parameters in Table 3 (bold values only). The legend refers to the table row IDs.

are approximately characterized by the hyperplane defined by:

$$q + 0.0077s_{\infty} - 0.054a = 2.61. \quad (31)$$

This indicates that, as long as (31) holds, the tensile curve simulated by the Sachs model will almost keep the same. Hence, q , s_{∞} and a are coupled here and cannot be determined by an inverse analysis based on the tensile curve only.

6.2. Advantage of the two-step optimization

In order to study the benefit of using the proposed two-step optimization, a CPFEM-based optimization was run using the parameters provided by ? as the initial guess, instead of using these provided by the Sachs-based method (see Table 1). This optimization is referred to as the direct CPFEM-based optimization (as opposed to the two-step optimization) hereafter. The task was stopped after the 14th iteration (i.e. 1400 h of computing). At the end of this optimization task, the optimized values were $q = 1.666$, $h_0 = 245.3$, $s_0 = 13.9$, $s_{\infty} = 140.8$, $a = 1.92$ and $\chi = 1.09 \times 10^{-2}$. As a reminder, the two-step optimization lead to $\chi = 1.06 \times 10^{-2}$ (see Table 2). This indicates that the minimum found by direct CPFEM-based optimization is not global. As a result, it is exposed to local minima, as well as the Sachs-based optimization. This confirms the hypothesis made by ?. One way to eliminate this issue is to use a multistart approach, as done with the Sach model (see section 6.1). However, this technique would be extremely time-consuming (a multistart approach with 8 different initial guesses would last about 130 days). Hence, the two-step optimization can help circumventing these limitations. Alternatively, one could use global optimization methods (?) instead of gradient-based approaches, like L-BFGS-B.

The convergence of the direct CPFEM-based optimization is illustrated in Figure 16. Here, the behaviour of the minimizer appears erratic at the early iterations (see Figure 9 for comparison), before slow convergence toward the final values. However, it is clear that the convergence is not reached before the 11th iteration. This indicates that the convergence is roughly 45% faster in the two-step optimization than in the direct CPFEM-based optimization (recall that only 6 iterations were required in the two-step optimization; see sec. 5.4.1). In Figure 16, the values of s_0 appear almost constant as long as the other parameters are not optimized; this phenomenon is consistent with that reported in the two-step optimization. It is worth pointing that the two-step and the direct optimizations lead to almost the same value for q (≈ 1.68).

6.3. Plastic activity

In this subsection, the plastic activity of each SS, computed from CPFEM in all grains, is investigated.

The slip activity can be studied thanks to CPFEM results. Figure 17 shows the traces of the 2 most active SSS within each grain (solid and dashed lines), according to CPFEM results. In order to evidence the consistency with

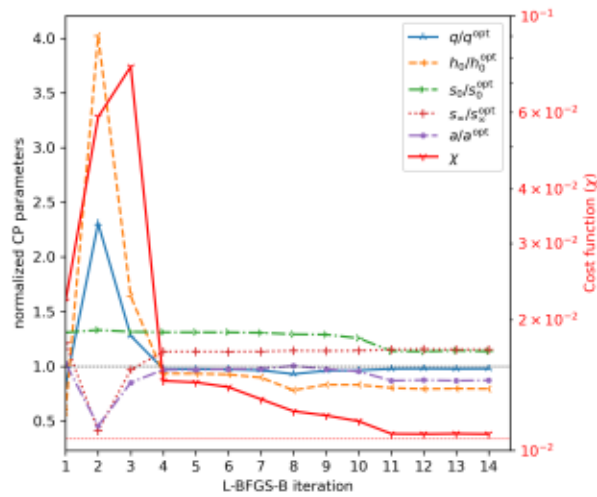


Figure 16: Evolution of the CP parameters and of the cost function (χ), depending on the iteration step of direct CPFEM-based optimization. Again, each CP parameter was normalized with respect to the optimal value (given in Table 2). Thin horizontal dashed lines represent the values calibrated by the two-step method.

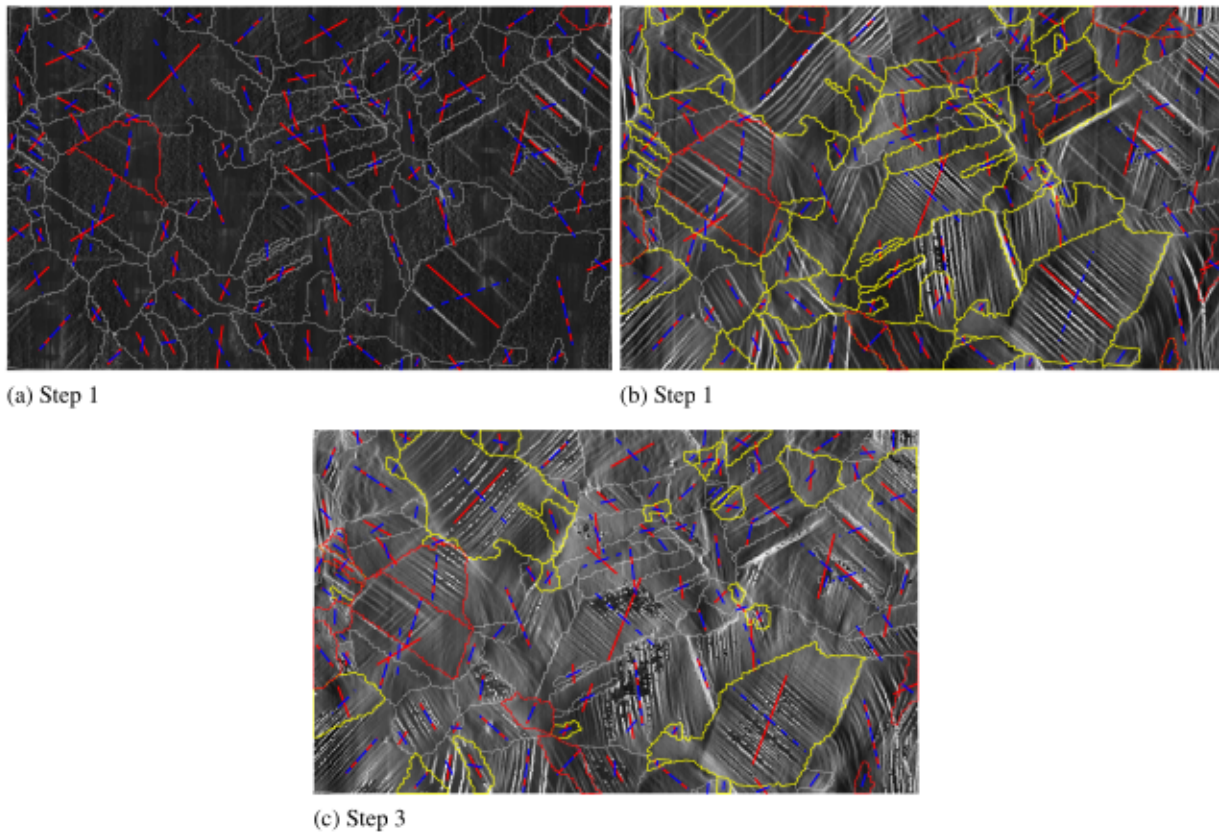


Figure 17: Slip activity within each grain, according to CPFEM simulations: the red solid straight lines represent the traces of the most active SSs; the blue dashed straight lines illustrate the 2nd most active. Experimental traces, evidenced through the criterion ϵ_{IGP} and taken from (?), are shown as greyscale backgrounds. Grains where a discrepancy between the experimental and the simulated slip traces exists are highlighted in red. In figure (b) and (c), grains where at least one of the two most active systems has changed compared to the previous step are highlighted (thick yellow GBs)

Table 4

Number of grains where none, one, or both of the two most active SSs change(s) between different steps.

	Step 1 to step 2	Step 2 to step 3
The two most active SSs are the same	61 grains	88 grains
1st is the same, the 2nd has changed	31 grains	17 grains
The 1st and 2nd have switched	12 grains	9 grains
The two most active SSs have changed	1 grains	1 grains
2nd is the same, the 1st has changed	none	none

experimental results, DIC measurements (with $\varphi = 1.3 \mu\text{m}$) are illustrated in the backgrounds of each map. Indeed, only few grains show discrepancy between the apparent and the simulated traces (highlighted in red in Figure 17). At most, 11 out of the 115 grains studied display inconsistent slip traces. This can be due to interaction with grains underneath the surface (?). It also appears that in some grains, the two most active SSs share the same trace (solid and dashed lines are parallel). This indicates that *apparent* simple slip can in fact result from double slip. This is consistent with experimental results made on other FCC materials, such as austenitic stainless steel (?) or Ni-based superalloy (?). In order to evidence the differences between steps 1, 2 and 3, grains where one of the two most active SSs has changed between step 1 and step 2, or between step 2 and step 3, are highlighted in Figures 17b and 17c. Table 4 sums up the number of grains evidencing such kind of changes. It appears that, between step 1 and step 2, almost one half of the grains undergo changes in at least one of the two most active SSs, indicating a kind of transient phenomenon. On the opposite, this proportion drops to 27% between steps 2 and 3, suggesting that the plastic behaviour enters a steady-state regime. Simulation at larger strain should be performed to accurately estimate the onset of this regime. It is worth noting that, as long as a grain undergoes a change in the most active SS, the 2nd most active changes as well. In some cases, the two most active SSs just switch between subsequent steps. All these changes can be related to the evolution of the stress state or to the rotation of the crystals. In a further work, all these analyses could be compared against experimental results by taking advantage of HREBSD technique (?) or identification of slip activity from SEM-DIC measurements (?).

6.4. On the use of ϵ_{eff} or ϵ_{IGP} in DIC

This section investigates the relevancy of using ϵ_{eff} (3) or ϵ_{IGP} (4) in DIC to estimate the equivalent strain.

Figure 18 illustrates the values of ϵ_{IGP} , estimated from CPFEM results, as 2D maps. It appears that the distribution of ϵ_{IGP} is very similar to that of the equivalent strain (see Figure 10 for comparison). In order to highlight the differences between ϵ_{eff} and ϵ_{IGP} , Figure 19 illustrates both the values as functions of the equivalent strain given by CPFEM (denoted ϵ_{eqv} below). In each scatter plot, linear regression was made (straight lines in Figure 19). As a result, it appears that using ϵ_{eff} , on average, leads to a 32% underestimation of the equivalent strain. Conversely, using ϵ_{IGP} leads to a 6% underestimation of the equivalent strain. The coefficient of determination when using ϵ_{eff} (resp. ϵ_{IGP})

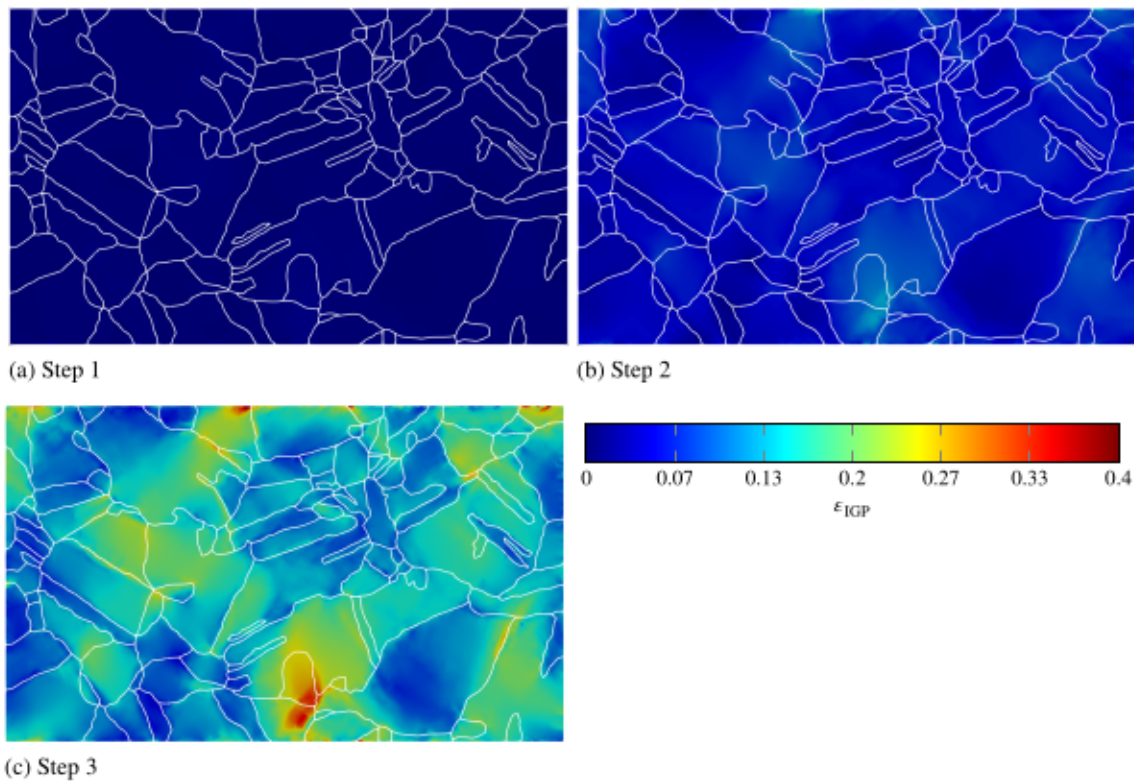


Figure 18: Maps of the equivalent strain, estimated under the IGP assumption from CPFEM results.

was $R^2 = 0.72$ (resp. 0.95). As a conclusion, ϵ_{IGP} appears to be a better criterion for the plastic strain, for it reduces both the systematic and the random errors when one tries to estimate the equivalent strain from DIC measurements.

In order to check consistency between experiment (DIC) and numerical results, Figure 20 illustrates the grain-wise mean values of all the criteria described above (namely ϵ_{eff} , ϵ_{IGP} and ϵ_{eqv}) estimated from CPFEM as functions of the ones found by DIC, as provided by ?. It appears that, whatever the function being used as a strain criterion, the discrepancy between DIC measurements and CPFEM can be very large. This is in accordance with the discussion made in section 5.4.2. In Figure 20, each dot is coloured depending on the surface of the corresponding grain. As a result, it appears that the smaller the grain, the larger the discrepancy. Linear regressions were made between experimental and simulated strain values, with each data point weighted by the grain surface. These regression are illustrated by straight dotted lines in Figure 20. Hence, the global trends are correct for all combinations, indicating that they are all consistent with each other. It is worth noticing that using grain-wise mean values considerably reduces the spreads (see Figure 11 for comparison). The best consistency is reached between ϵ_{eqv} from CPFEM and ϵ_{IGP} from DIC. This indicates that ϵ_{IGP} is an accurate criterion for estimating the strain by DIC. According to the slope (denoted k in Figure 20), on average, values of ϵ_{IGP} computed from DIC underestimate the equivalent strain by 1.2%.

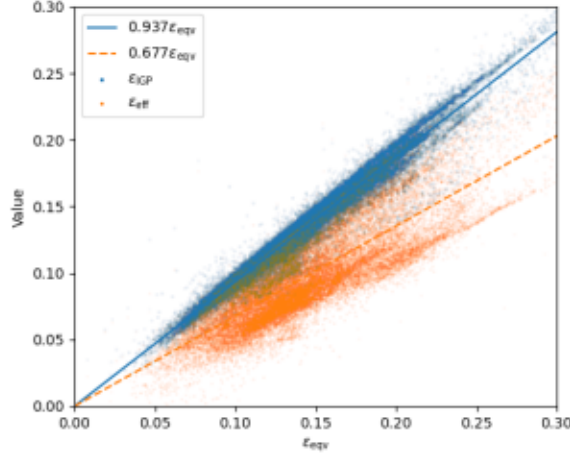


Figure 19: Equivalent strain criteria estimated from CPFEM simulations: plot of ϵ_{eff} (3) or ϵ_{IGP} (4) as functions of the overall equivalent strain strain (ϵ_{eqv}). Straight lines give the results from linear regressions.

It was demonstrated in section 6.3 that the traces of the most active slip systems in CPFEM are consistent with the DIC measurement made with window size $\varphi = 1.3 \mu\text{m}$ (Fig. 3a); conversely, the strain measurement made with $\varphi = 9.6 \mu\text{m}$ (Fig. 3b) show some discrepancies with CPFEM results, specially for smaller grains. This suggests that this accuracy can be due to the window size used in DIC. However, additional numerical simulations need to be done in order to investigate the influence of the microstructure underneath, which can also impair the strain (??).

6.5. Toward a path-dependent plastic criterion in DIC

In this section, a generalization of the plastic criterion ϵ_{IGP} , as introduced by ?, is proposed to make it path-dependent. Its values are compared against ϵ_{IGP} .

Under the IGP assumption, the strain rate tensor (10a) is:

$$\dot{\epsilon} = \begin{bmatrix} \dot{\epsilon}_{11} & \dot{\epsilon}_{12} & 0 \\ \dot{\epsilon}_{12} & \dot{\epsilon}_{22} & 0 \\ 0 & 0 & -\dot{\epsilon}_{11} - \dot{\epsilon}_{22} \end{bmatrix}. \quad (32)$$

Thus, the equivalent strain rate is:

$$\begin{aligned} \dot{\epsilon} &= \sqrt{\frac{2}{3} \dot{\epsilon}_{ij} \dot{\epsilon}_{ij}} \\ &= \frac{2}{\sqrt{3}} \sqrt{\dot{\epsilon}_{11}^2 + \dot{\epsilon}_{22}^2 + \dot{\epsilon}_{12}^2 + \dot{\epsilon}_{11} \dot{\epsilon}_{22}} \end{aligned}$$

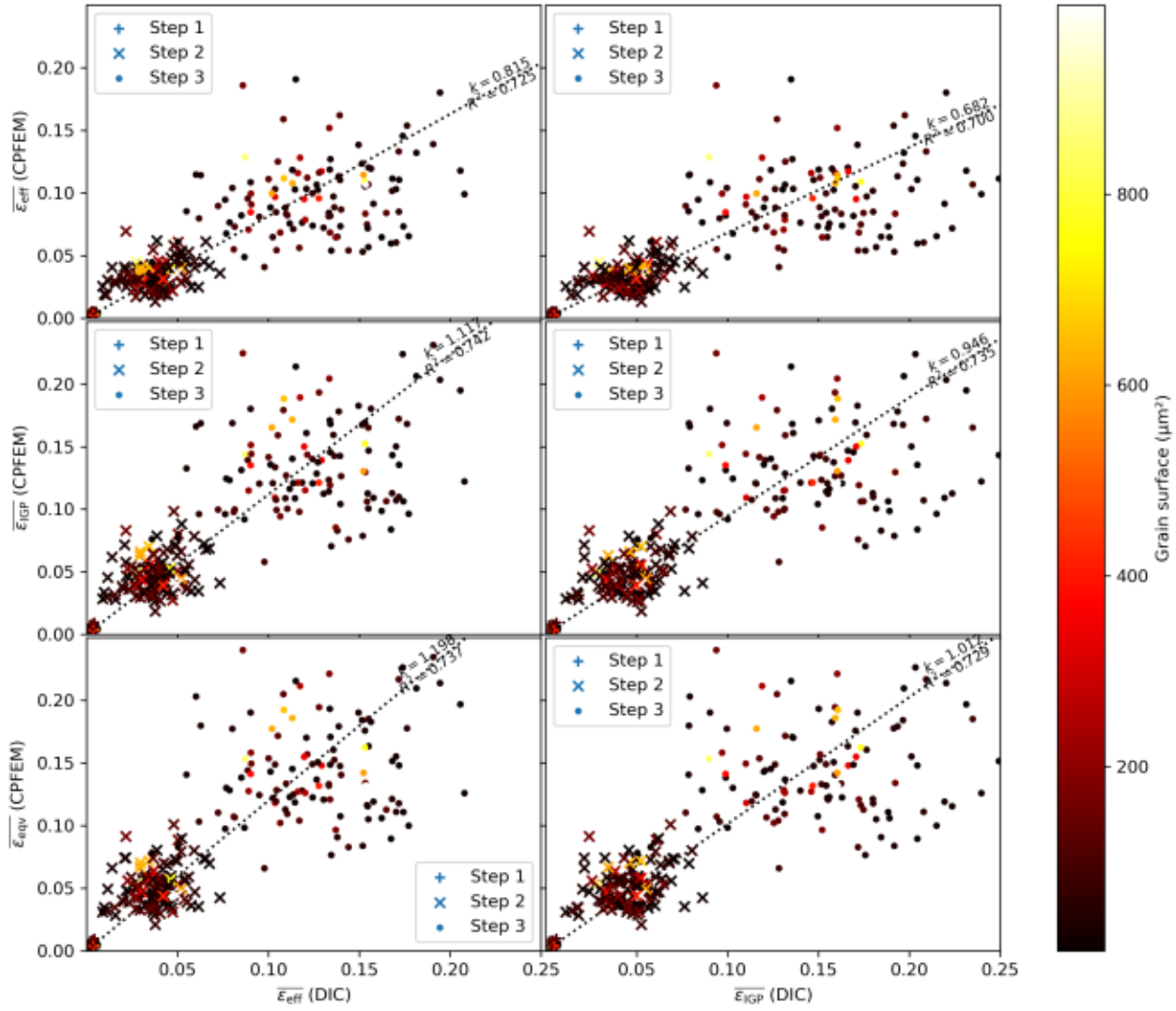


Figure 20: Grain-wise mean values of plastic criteria given by CPFEM, as compared with the experimental values given by DIC (?). The colour relates to the apparent grain surface. Dotted line illustrates results from the grain surface-weighted linear regressions: the slopes (k) and the residuals (R^2) are given.

In (32), the strain rate is defined as the symmetric part of the Eulerian velocity gradient, such that:

$$\dot{\varepsilon}_{ij} = \frac{1}{2} \left(\frac{\partial v_i}{\partial x_j} + \frac{\partial v_j}{\partial x_i} \right) \quad (33)$$

where v_i is the material velocity along the i -th direction. It reads:

$$\frac{\partial v_i}{\partial x_j} = \frac{\partial v_i}{\partial X_k} \frac{\partial X_k}{\partial x_j} = \frac{\partial F_{ik}}{\partial t} \tilde{F}_{kj}$$

where \tilde{F}_{kj} denotes the kj -th component of the inverse gradient tensor ($\tilde{\mathbf{F}} = \mathbf{F}^{-1}$). Under the IGP assumption (5), we have (?):

$$\begin{aligned}\tilde{\mathbf{F}} &= \begin{bmatrix} F_{11} & F_{12} & 0 \\ F_{21} & F_{22} & 0 \\ 0 & 0 & 1/D \end{bmatrix}^{-1} \\ &= \begin{bmatrix} F_{22}/D & -F_{12}/D & 0 \\ -F_{21}/D & F_{11}/D & 0 \\ 0 & 0 & D \end{bmatrix}\end{aligned}$$

with $D = F_{11}F_{22} - F_{12}F_{21}$. Let Δt be the time interval between two subsequent time steps $(\theta - 1)$ and θ ; the average strain rate can be estimated as:

$$\dot{\varepsilon}_{ij}^{\theta} \approx \frac{\Delta F_{ik}^{\theta} \tilde{F}_{kj}^{\theta} + \Delta F_{jk}^{\theta} \tilde{F}_{ki}^{\theta}}{2\Delta t} \quad (34)$$

with

$$\Delta F_{ij}^{\theta} = \begin{cases} F_{ij}^{\theta} - \delta_{ij} & \text{if } \theta = 1, \\ F_{ij}^{\theta} - F_{ij}^{\theta-1} & \text{otherwise.} \end{cases} \quad (35)$$

In Eqs. (34) and (35), F_{ij}^{θ} and \tilde{F}_{ij}^{θ} denote the ij -th component at step θ of gradient and inverse gradient tensors, respectively. The cumulative equivalent strain is the integral over time of the equivalent plastic strain rate:

$$\varepsilon_{\text{eqv}} = \int_0^t \dot{\varepsilon} dt$$

As a result, the path-dependent equivalent strain, estimated under the IGP assumption, can be defined as:

$$\varepsilon_{\text{IGP,PD}} = \sum_{\theta=1}^{n_{\text{step}}} \dot{\varepsilon}^{\theta} \Delta t = \sum_{\theta=1}^{n_{\text{step}}} \Delta \bar{\varepsilon}^{\theta} \quad (36)$$

with

$$\Delta \bar{\varepsilon}^{\theta} = \frac{2}{\sqrt{3}} \sqrt{(\delta \varepsilon_{11})^2 + (\delta \varepsilon_{22})^2 + (\delta \varepsilon_{12})^2 + \delta \varepsilon_{11} \delta \varepsilon_{22}}$$

and

$$\begin{aligned}\delta\varepsilon_{11} &= \Delta F_{11}^\theta \tilde{F}_{11}^\theta + \Delta F_{12}^\theta \tilde{F}_{21}^\theta, \\ \delta\varepsilon_{22} &= \Delta F_{21}^\theta \tilde{F}_{12}^\theta + \Delta F_{22}^\theta \tilde{F}_{22}^\theta, \\ \delta\varepsilon_{12} &= \frac{\Delta F_{11}^\theta \tilde{F}_{12}^\theta + \Delta F_{12}^\theta \tilde{F}_{22}^\theta + \Delta F_{21}^\theta \tilde{F}_{11}^\theta + \Delta F_{22}^\theta \tilde{F}_{21}^\theta}{2}.\end{aligned}$$

It is worth mentioning that $\varepsilon_{\text{IGP,PD}}$ relates to the true strain whereas ε_{IGP} relates to the engineering strain (Chap. 2). Therefore, Figure 21 illustrates the values of $\varepsilon_{\text{IGP,PD}}$ as a function of $\log(1 + \varepsilon_{\text{IGP}})$. It appears that both the criteria lead

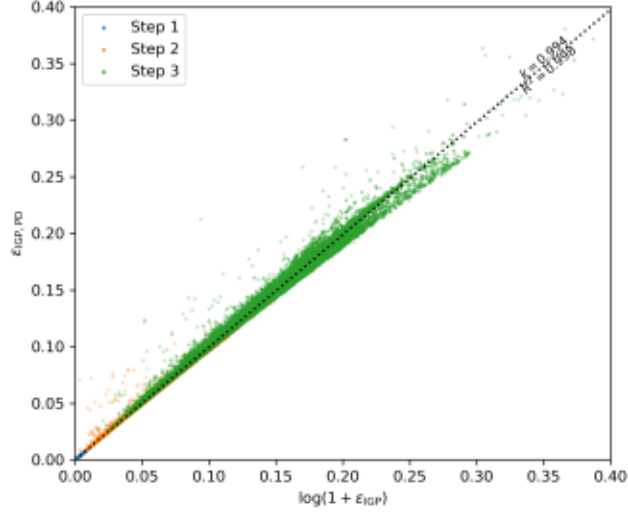


Figure 21: Values of $\varepsilon_{\text{IGP,PD}}$ (36) as a function of the true strain estimated from ε_{IGP} (4), computed from CPFEM results. The dotted line illustrates the linear regression.

to very similar true equivalent strains. The linear regression shows that, on average, $\varepsilon_{\text{IGP,PD}}$ is 0.6% smaller than the true strain estimated from ε_{IGP} . As a conclusion, using $\varepsilon_{\text{IGP,PD}}$ or ε_{IGP} for evaluating the plastic strain has little effects here because both descriptors lead to very similar results. However, it is worth pointing that, in case of non-monotonic loading (e.g. cyclic loading), the path-dependent criterion $\varepsilon_{\text{IGP,PD}}$ may be preferable. This also applies in case of large strain (>0.5) for $\varepsilon_{\text{IGP,PD}}$ relates to the true strain, as long as the strain is small enough ($\varepsilon_{\text{IGP}} < 0.2$ here). This threshold value may depend on the number of steps; further analyses, with a larger number of steps, need to be done to check this hypothesis.

6.6. Influence of the number of orientations in simulations

The influence of the number of orientations used for the Sachs model is investigated in this subsection.

As seen in section 5.4, the number of grains used in CPFEM seems too low to correctly estimate the texture evolution. Thus, the Sachs model was used to compute the texture evolution, starting from the 115 mean orientations

of the grains. The corresponding results are referred to as the Reduced Data -Sachs model (RD-Sachs) hereafter. As a reminder, 1000 unique orientations, randomly picked from EBSD data, were used in the full Sachs model (see sec. 4.2). Figure 22 illustrates the results of the RD-Sachs model in terms of tensile curve. For the sake of comparison, experimental data and results from the full Sachs model are recalled (blue dots and orange solid line, respectively). As a

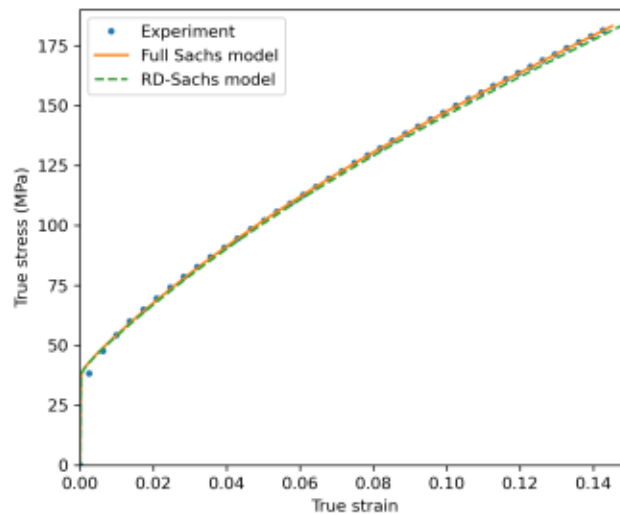


Figure 22: Tensile curve obtained using the RD-Sachs model (dashed line).

result, considering only grain-wise mean orientations, instead of all orientations given by EBSD, has very little effect on the macroscopic behaviour. Figure 23 illustrates the results of the RD-Sachs model in terms of crystallographic texture. It appears that the texture evolution is really different with the RD-Sachs model, compared to the full Sachs

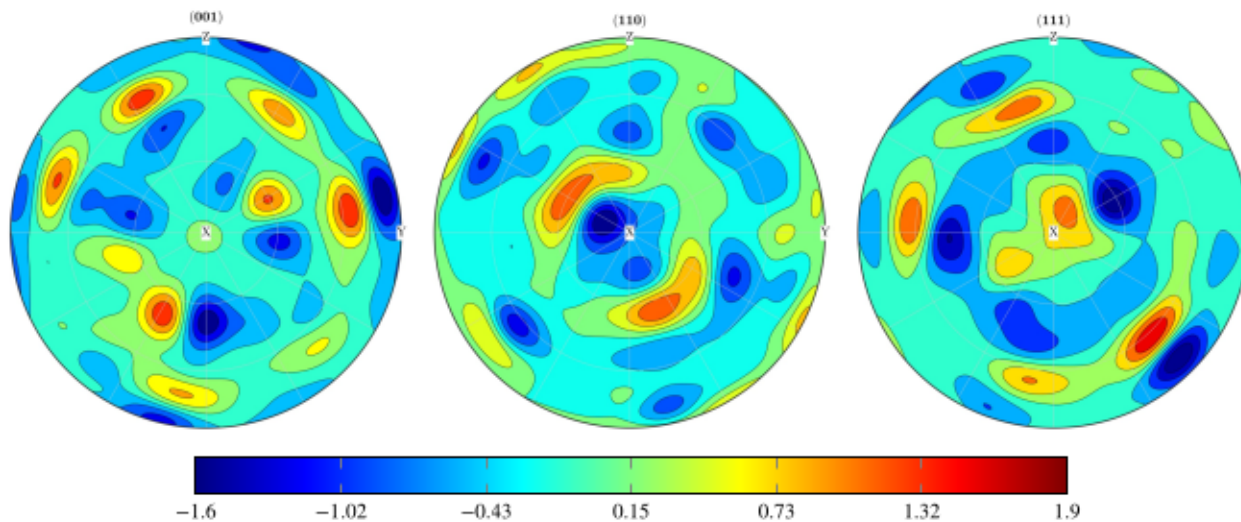


Figure 23: PFs of changes in texture (ΔODF), given by the RD-Sachs model (TI: 1.02).

(see Figure 5a for comparison). However, the PFs in this case display similar patterns with these obtained from CPFEM

(see Fig. 14). Again, it is worth mentioning that the texture evolution seems very sharp compared to the CPFEM and the experimental results. This can also be evidenced by the high TI (1.02). However, this analysis confirms that 115 grains are not enough for analysing the full texture evolution and that the “missing” texture components in CPFEM (as reported in section 5.4.2) can be attributed to the number of considered grains.

7. Conclusion

The first objective of this paper was to propose a robust technique to identify the Crystal Plasticity (CP) parameters from in situ tensile tests, which can be run within a reasonable time. First, a simple and fast Sachs-based model has been proposed to simulate the elasto-plastic behaviour of polycrystalline aggregates. It was shown that this model is able to well predict the evolution of crystallographic texture during tensile test, albeit its apparent simplicity and the strong hypotheses it is based on. This model was used to find the CP parameters of pure copper through an inverse analysis scheme, based on the tensile curve. This inverse analysis can be exposed to local minimal issues, which can be circumvented by a multistart approach. Nevertheless, this technique does not ensure uniqueness of the optimized parameters, hence the need for another inverse analysis based on full-fields measurements. Thus, a second optimization step has been proposed, based on CPFEM simulations and in situ full-field measurements. The estimator found at the previous step was used as the initial guess of the CPFEM-based inverse analysis, allowing the minimizer (L-BFGS-B algorithm) to quickly converge toward the optimal value. It was shown that CPFEM-based optimization is exposed to local minima as well, but the multistart approach is not feasible in this case because of very large running time it would require. Hence, a proposed methodology is to get a first sight on optimal values using a fast model; then to optimize these values through CPFEM-based optimization. The “fast” model used here was that of Sachs, but others, like FFT-based (?) or VPSC methods (??) could be used as well.

The second objective of this paper was to compare the results obtained by CPFEM against experiments. The following statements were made:

- the heterogeneous distribution of strain between grains is consistent with the experimental results, although some discrepancies have been evidenced at sub-grain scale;
- parallel traces of slip planes within each grain, evidenced by SEM DIC, can in fact result from double slip;
- the CPFEM model predicts well the slip activity (i.e. tailoring the question “*which slip system is the most active?*”);

The relevancy of using ϵ_{eff} (as defined by ?) or ϵ_{IGP} (as defined by ?) to evidence the localization bands by DIC was also studied. It was shown that the latter is a better choice for two reasons: it leads to better consistency between experimental measurements (from DIC) and numerical simulations, and its values are closer to the equivalent strain

(ϵ_{eqv}) given by CPFEM. On average, ϵ_{IGP} values computed from DIC measurements lead to 1.2% underestimation of the equivalent strain. A generalization of ϵ_{IGP} to make it path-dependent was proposed (denoted $\epsilon_{\text{IGP,PD}}$ (36) above). It was shown that, in the present work, ϵ_{IGP} and $\epsilon_{\text{IGP,PD}}$ lead to very similar results. However, $\epsilon_{\text{IGP,PD}}$ should be used for evidencing plastic strain from in situ SEM-DIC measurements in case of non-monotonic straining or larger strain. Further analyses, similar to these presented in section 6.4, should be performed to assess such criterion in this case.

It was demonstrated that strain values measured by DIC can be inconsistent with these estimated by CPFEM. The two possible culprits for this are:

- the window size used in DIC, which needs to be small enough, compared to the grain size;
- the underneath microstructure, which can impair the local mechanical behaviour.

Thus, further analyses, involving thin-layer removal, may be performed in order to investigate the microstructure underneath; such analysis will involve additional numerical simulations as well. In a future work, the use of global optimization methods, instead of L-BFGS-B, could be investigated. The influence of the definition for the cost functions could also be studied. For instance, the kinematic cost function could be improved to focus on activities of each slip system, by taking into account the local crystallographic reorientations. Clues about a possible implementation of such an approach are provided in Appendix C.

CRediT authorship contribution statement

D. Depriester: Conceptualization of this study, Software, Validation, Formal analysis, Writing - Original Draft.
J.P. Goulmy: Investigation, Writing - Original Draft. **L. Barrallier:** Writing - Review & Editing, Supervision.

A. Mean elastic behaviour of polycrystalline aggregates

This subsection sums up the Voigt, Reuss and Hill averaging methods for estimating the macroscopic stiffness tensor of a polycrystal.

Let σ be the Cauchy's stress tensor and ϵ^e be the small strain elastic tensor. Assuming linear elasticity, the generalized Hooke's law gives:

$$\sigma = c : \epsilon^e \quad (37)$$

where c denotes the 4th order stiffness tensor and ":" stands for the tensor product contracted two times. Using the Einstein's summation convention, (37) is equivalent to:

$$\sigma_{ij} = c_{ijkl} \epsilon_{kl}^e.$$

If the aggregate consists in n_C unique crystals, the Voigt average for stiffness tensor is:

$$c^V = \frac{1}{n_C} \sum_{r=1}^{n_C} c^{(r)}$$

where $c^{(r)}$ is the rotated stiffness tensor, so that:

$$c_{ijkl}^{(r)} = G_{ijklmnop}^{(r)} c_{mnop}$$

$G_{ijklmnop}^{(r)}$ denotes the components of the 8th order rotation tensor $G^{(r)}$. They can be defined depending on the components of the orientation matrix $g^{(r)}$ of crystal r (?):

$$G_{ijklmnop}^{(r)} = g_{mi}^{(r)} g_{nj}^{(r)} g_{ok}^{(r)} g_{pl}^{(r)}$$

Likewise, the Reuss average for stiffness tensor is the inverse of the mean compliance tensor:

$$c^R = \left(\frac{1}{n_C} \sum_{r=1}^{n_C} s^{(r)} \right)^{-1}$$

with

$$s_{ijkl}^{(r)} = G_{ijklmnop}^{(r)} c_{mnop}^{-1}$$

The arithmetic average for stiffness tensor proposed by ? is:

$$c^H = \frac{1}{2} (c^V + c^R) . \tag{38}$$

It is well known that this average provides good approximation for the elastic behaviour of bulk materials (e.g. ???).

Hence, the macroscopic elastic strain can be estimated as follows:

$$\epsilon^e = (c^H)^{-1} : \sigma$$

B. Projection of node displacements to DIC measurement locations

This section briefly describes the proposed method to map the displacement field given at mesh nodes onto possibly inconsistent locations, where DIC measurements are actually made. This method is based on the Delaunay triangulation

(?) performed from node locations, as illustrated in Figure 24. Let P be the location where one wants to estimate the

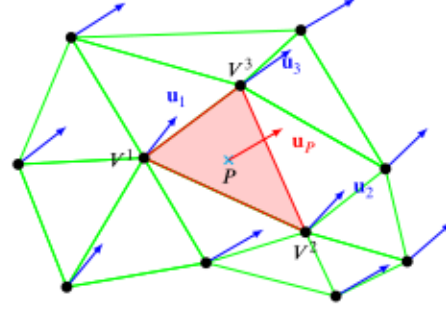


Figure 24: Representation of the triangulation procedure, used for estimating the displacement at random location P (cyan cross). Black dots represent the mesh nodes, where the displacement are given by CPFEM (blue arrows). The green lines illustrate the triangles from Delaunay triangulation, whereas the red area highlights the triangle P belongs to.

displacement, given the node displacements. The proposed algorithm can be summarized as follows:

1. apply the Delaunay triangulation on mesh nodes,
2. find which triangle P belongs to,
3. compute the coordinates (denoted $(\tilde{P}_1, \tilde{P}_2)$ below) of this point, with respect to its parent triangle,
4. from these coordinates, find weights $(\phi^1, \phi^2$ and $\phi^3)$ corresponding to each vertex of the parent triangle,
5. compute the weighted arithmetic mean of displacements at these vertices.

In details, let V^1 , V^2 , and V^3 be the vertices of the identified parent triangle. The coordinate transformation matrix related to this triangle is:

$$\mathbf{M}^{\text{tri}} = \begin{bmatrix} V_1^2 - V_1^1 & V_1^3 - V_1^1 \\ V_2^2 - V_2^1 & V_2^3 - V_2^1 \end{bmatrix}$$

where V_j^i denotes the j -th coordinate of vertex V^i . The local coordinates of P are:

$$\begin{bmatrix} \tilde{P}_1 \\ \tilde{P}_2 \end{bmatrix} = (\mathbf{M}^{\text{tri}})^{-1} \begin{bmatrix} P_1 - V_1^1 \\ P_2 - V_2^1 \end{bmatrix}$$

Thus, the weights are computed as in a FEM linear triangle (?, Chap. 9):

$$\phi^1 = 1 - \tilde{P}_1 - \tilde{P}_2 \quad (39a)$$

$$\phi^2 = \tilde{P}_1 \quad (39b)$$

$$\phi^3 = \tilde{P}_2 \quad (39c)$$

and finally, the projected displacement at P is:

$$\mathbf{u}^P = \sum_i \phi^i \mathbf{u}^i \quad (40)$$

where \mathbf{u}^i is the displacement of vertex V^i , as illustrated in Figure 24.

C. Toward a crystallographic orientation -based cost function

This section describes a possible scheme for defining a cost function (as defined in section 5.2) based on the difference in crystallographic orientations between experimental and simulation data, and the related technical difficulties one should circumvent to perform such analysis.

C.1. Triangular projection of orientations

The first difficulty lies in the fact that quadrature points (Gauss points), where the crystallographic orientations are computed by CPFEM, have inconsistent locations with these of EBSD mapping. Therefore, it is necessary to project the orientation field given by EBSD onto quadrature locations. Following the same procedure as for displacement fields (see Appendix B), one should project the measured orientations. Let \mathbf{g}^1 , \mathbf{g}^2 and \mathbf{g}^3 be the crystallographic orientations⁹ measured at locations V^1 , V^2 and V^3 , respectively (see Figure 24). In order to compute the weighted mean of \mathbf{g}^1 , \mathbf{g}^2 and \mathbf{g}^3 , the easiest way is to use the related unit quaternions \mathbf{q}^1 , \mathbf{q}^2 and \mathbf{q}^3 (?). ? demonstrated that the weighted mean quaternion $\bar{\mathbf{q}}$ is defined as the principal axis of matrix \mathbf{Q} , with:

$$\mathbf{Q} = \sum_{i=1}^3 \phi^i \mathbf{q}^i (\mathbf{q}^i)^\top . \quad (41)$$

Then, $\bar{\mathbf{q}}$ can be converted back to orientation to get the weighted mean of \mathbf{g}^1 , \mathbf{g}^2 and \mathbf{g}^3 .

C.2. Orientation error

Considering a quadrature point P in the mesh, let $\mathbf{g}_{\text{EBSD}}^P$ be the measured orientation, projected at P , and $\mathbf{g}_{\text{FEM}}^P$ be the corresponding orientation given by CPFEM. If $\mathbf{g}_{\text{EBSD}}^P$ and $\mathbf{g}_{\text{FEM}}^P$ are expressed as rotation matrices, the distance between them, also known as the misorientation angle, is (?):

$$\theta^P = \min_{\mathbf{s} \in \mathcal{S}} \omega \left((\mathbf{g}_{\text{EBSD}}^P)^{-1} \mathbf{g}_{\text{FEM}}^P \mathbf{s} \right)$$

⁹Here, "orientation" can refer to any way to represent an orientation (Euler angles, rotation matrix, Rodrigues vector...).

where S is the set of crystallographic symmetry equivalent transformations and $\omega(\mathbf{m})$ is the magnitude of rotation matrix \mathbf{m} , so that:

$$\omega(\mathbf{m}) = \arccos\left(\frac{\text{trace}(\mathbf{m}) - 1}{2}\right). \quad (42)$$

Finally, a normalized cost function, related to the error in crystallographic orientation, could be:

$$\chi^{\#} = \frac{1}{N} \sum_P \frac{\theta^P}{\theta_{\max}}$$

where N is the number of quadrature points and θ_{\max} is the maximum possible misorientation angle owing to the crystal symmetry (e.g. 62.8° for cubic).

References